International Journal of Mining Science and Technology 35 (2025) 1753–1773

Contents lists available at ScienceDirect

International Journal of Mining Science and Technology

journal homepage: www.elsevier.com/locate/ijmst

Quantitative characterization of fracture surface undulations and gas-guiding patterns in fractured rocks under steady loading

Zihan Chen [a,b], Quanle Zou [a,*], Feixiang Lv [a], Qican Ran [a], Xiaoyan Sun [c], Xianwei Heng [d]

[a] *State Key Laboratory of Coal Mine Disaster Dynamics and Control, School of Resources and Safety Engineering, Chongqing University, Chongqing 400044, China*
[b] *NBK Institute of Mining Engineering, University of British Columbia, Vancouver V6T 1Z4, Canada*
[c] *School of Resources and Safety Engineering, Henan University of Engineering, Zhengzhou 451191, China*
[d] *Guizhou Province Mine Safety Science Research Institute Co., Ltd., Guiyang 550000, China*

ARTICLE INFO

Article history:
Received 7 March 2025
Received in revised form 14 June 2025
Accepted 30 August 2025
Available online 15 October 2025

Keywords:
Tensile damage
Fracture surface roughness
Pattern of undulation
Gas-guiding process
Flow characteristics

ABSTRACT

Fractures in rock strata serve as flow pathways for gas flow. The undulation of fracture channels can influence the guidance of gas flow. In this context, four-point bending experiments on prefabricated fractured rocks at different angles under stable stepped loading stress. The experiment results clarified the evolutionary law that the undulation degree of the rock tensile fracture surface is separated by an initial fracture angle of 45°. The high undulation intervals were less than 45°, whereas the low undulation intervals were more than 45°. Furthermore, the relative undulation degree, undulation frequency, and matching degree of the fracture surface were quantified. The relationship between the change in fracture surface undulation and gas flow guidance was established. Based on this, the stability, tortuosity, and uniformity of the gas flow in the fracture channel were quantitatively characterized. Subsequently, numerical models of the fracture channels were constructed to validate the indices proposed in this study. The results of the study clarified the influence of different initial fracture angles on the undulation changes of fracture surfaces, and established the relationship between these changes and gas flow, which is conducive to understanding the role of internal fracture channels in rocks in guiding the gas flow process.

1. Introduction

During coal mining, the original stress state in the overlying rock strata is disrupted [1]. This leads to the collapse of the overlying rock strata in the goaf after the coal mining is completed. The immediate roof bends and subsides [2], forming a fractured rock beam structure [3], as shown in Fig. 1. Moreover, after the coal seam is mined, long-term stable stress acts on the rock strata overlying the goaf. The rock strata gradually fracture under long-term stable stress, resulting in tensile damage [4] and internal fracturing within the rock strata. Gas residual in the goaf after mining of a coal seam or gas desorbed from coal and coal pillars will spread along the fractures of the overlying rock strata in the goaf [5,6]. Additionally, fractures in the overlying rock strata of the goaf act as channels for gas to migrate upward [7]. Consequently, both the morphology and roughness of the fracture surfaces can interfere with the gas flow process. It, in turn, affects the distribution and diffusion of gas within the overlying strata of the goaf. Additionally, due to the impact of coal mining, fractures are included in the overlying strata of the goaf. The existence of these fractures not only influences the fracturing of the rock strata but also further impacts the fracture development pattern. Hence, to clarify the distribution and expansion pattern of gas in the overlying rock strata of the goaf, it is necessary to quantify the fracture morphology of the overlying rock strata of the mining zone after fracture and its surface roughness and to elucidate the guiding effect of the fracture surface on the gas flow.

Fractures in rock strata serve as the primary channels for gas flow, and their morphology directly influences the direction of the gas flow. The mining process causes disturbances to the rock strata, resulting in fractures within the strata. The presence of these initial fractures alters the strength of the rock strata and the direction of the fracture extension. Currently, scholars have conducted research by using prefabricated fracture specimens to simulate rocks in a state with initial fractures. Jiang et al. [8] indicated that the fractures in prefabricated fracture specimens all originated from the tips of the initial fractures. Wang et al. [9] investigated the interactions between internal fractures within rocks during the uniaxial compression process. When the ratio of the fracture spacing to the fracture length was less than 1.5, the interaction between the fractures was pronounced. Conversely,

---

* Corresponding author.
E-mail address: quanlezou2011@126.com (Q. Zou).

https://doi.org/10.1016/j.ijmst.2025.08.017
2095-2686/

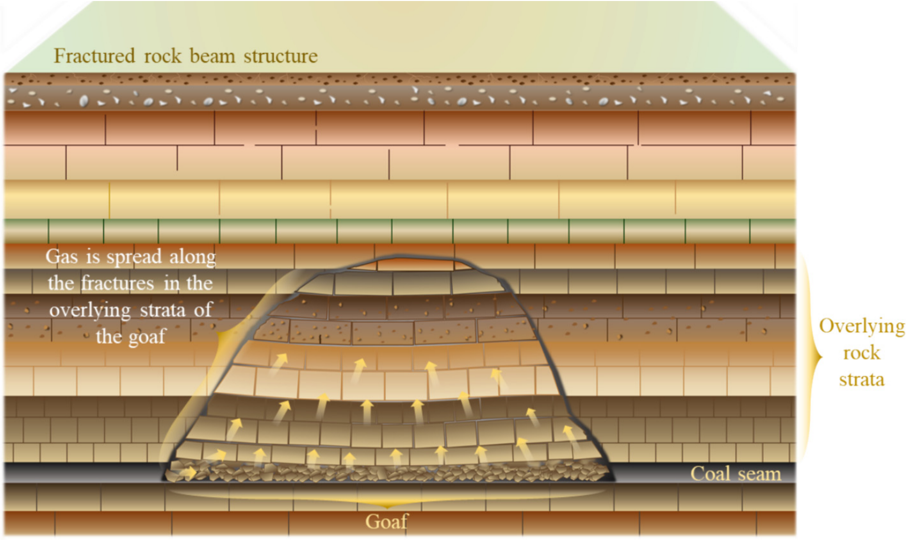

Fig. 1. Fractured rock beam structure.

the influence waned, and the growth rate of the wing fractures decelerated. Zhou et al. [10] utilized digital image correlation (DIC) and the discrete element method (DEM) to explore the fracture development status of conjugate fractures under uniaxial compression. The geometric configuration of conjugate fractures affected the location where fracture clusters develop within rock specimens. In rock specimens featuring conjugate fractures, the fracture development was predominantly concentrated in the lower portion of the specimen. Huang et al. [11] employed CT scanning to examine the internal fracture characteristics of rock specimens with double fractures. During the specimen failure process under high confining pressure, the number of vertical fractures increased. In contrast, under low confining pressure, horizontal fractures became more conspicuous during the specimen failure process. Li et al. [12] utilized an infrared monitoring system to capture the energy evolution during the failure process of fractured rocks in real time. Their research revealed that the formation of secondary fractures before and after the instability failure of rock specimens with prefabricated fractures resulted in sharp fluctuations in energy. Mu et al. [13] conducted uniaxial compression experiments on rock specimens with prefabricated fractures and varying angles. The research outcomes demonstrated that the presence of prefabricated fractures exerted a substantial influence on rock strength, and the damage became more severe as the fracture angle diminished. The studies mentioned above probed the fracture development and failure processes of rocks under compressive loads. Nevertheless, in the overlying strata of a goaf, the rock strata are subjected to stress from the overlying strata, leading to bending, tensile failure, and fracturing [14]. Hence, it is essential to analyze the fracture development process of fractured rocks under tensile loads. Xia et al. [15] applied a high-speed camera and a convolutional neural network (CNN) algorithm to monitor and forecast the fracture development process of rock specimens in a three-point bending test. Lu et al. [16] developed a microscopic visualization experimental setup to monitor the fracture development during the three-point bending test. It was revealed that, at the microscopic scale, fractures originated at multiple sites along the tips of the prefabricated fractures. These fractures then continued to expand and intertwine until a dominant fracture was eventually formed. Sarkar et al. [17] employed the semicircular bend (SCB) test in tandem with numerical analysis techniques. Their calculations showed that the elongation of the prefabricated fractures resulted in a reduction in fracture toughness. Gao et al. [18] augmented the number of prefabricated fractures and carried out three-point bending tests on specimens with double prefabricated fractures. They discovered that microfractures emerged precisely at the locations of the prefabricated fractures. Moreover, specimens with double fractures exhibited superior fracture resistance compared to those with a single fracture. The existence of initial fractures exerts a substantial influence on the development of fractures within the rocks. Consequently, researching on the internal fracture propagation in rocks with initial fractures can provide a more accurate depiction of the fracture morphology of rocks after breakage.

Meanwhile, the interior of rocks is composed of numerous tiny crystals [19,20], making the surfaces on either side of the fracture channels rough rather than smooth. This rough, undulating surface can affect the flow of gas. Li et al. [21] proposed that, compared to smooth fracture surfaces, rough fracture surfaces facilitate solute transport and mixing more effectively during fluid flow. Crandall et al. [22] utilized CT imaging to reconstruct a rough fracture surface and analyze the fluid flow pattern. Their research demonstrated that fluids exhibit tortuous flow paths under conditions of high joint roughness and fractal dimensions. The undulations of the fracture surface play a crucial role in guiding the gas flow, underscoring the need to quantify these undulations. In the field of quantification of fracture surface roughness, the joint roughness coefficient (JRC) [23] method has gained recognition from the International Society for Rock Mechanics. It measures the sliding inclination angle via an inclination experiment and back-calculates surface roughness using Barton's empirical formula for fracture surface strength. However, the JRC method is mainly applicable in two-dimensional (2D) calculations. For studying undulations in a three-dimensional (3D) perspective, the cubic covering method (CCM) [24] is more advantageous. Based on fractal geometry, CCM uses cubes of varying sizes to cover the 3D surface and computes the fractal dimension, where a larger value indicates more pronounced and higher roughness. Nevertheless, CCM has accuracy limitations when applied to the study of small-scale fracture surfaces. With the advancement of scanning technology, 3D scanning equipment [25] now enables the extraction of point cloud data from the fracture surface with a remarkably high level of accuracy [26]. As technology has advanced, scholars have proposed the surface area method (SAM) for quantifying the roughness of complex surfaces like rock fractures. Similar to CCM, SAM [24] relies on fractal geometry, calculating the fractal dimension by relating surface area to measurement scale and then evaluating roughness. Overall, scholars have developed quantification approaches from diverse dimensions and scales to quantify the overall roughness of rock surfaces. However, the calculation method still primarily focuses on surface roughness, and the relationship between roughness and gas flow remains unclear. Therefore, elucidating how changes in fracture surface undulation affect gas flow and quantifying this relationship will help define the role of roughness in guiding gas flow.

In this regard, this study conducted four-point bending experiments on rocks with prefabricated fractures at different angles under stable stepped loading stress. Fracture morphologies of the fractured rocks were analyzed, and high-precision scanning was performed on the fracture surfaces to extract their point cloud data. A series of indices related to the fracture surface, including the relative undulation degree, undulation frequency, and meshing degree, was proposed. These indices enable the quantification and characterization of stability, tortuosity, and uniformity of gas flow within the fracture channels based on surface roughness. Finally, the gas flow process in the fracture channels was validated by integrating the numerical models. The research findings investigated the impact of varying initial fracture angles on the undulation of fracture surfaces, and established a relationship between the fracture surface undulation and gas flow, providing a potential research perspective for understanding gas flow in the overlying rocks of goafs. These results will help analyze gas flow in the fractures of the overlying rock strata in the goafs, and further provide a reference for clarifying the diffusion and distribution of gas in the overlying rock strata after the mining stops at the working faces.

2. Experimental specimens and a four-point bending stable stepped loading system

2.1. Sandstone specimens

As shown in Fig. 2a, the four-point bending test specimens consisted of cuboid-shaped sandstone specimens with dimensions of 220 mm × 40 mm × 20 mm [27]. As shown in Fig. 2b, the main mineral composition of the specimen is SiO_2. In addition, the bedding plane of the specimen is horizontal. At the midpoint of the specimen (110 mm from each end), fractures of different angles were prefabricated, penetrating the specimen front to back. Each fracture had a total length of 8 mm and a width of 2 mm. The fracture angle, designated as α, is defined as the angle between the fracture vector and its base plane. The fracture was cut with a fine wire to minimize disturbance to the rock during cutting. To conduct a comprehensive and in-depth investigation into the effects of diverse fracture angles on the morphological characteristics and surface roughness of the fracture channels, a series of prefabricated fracture angles was set. These angles are specified as $\alpha = 0°$, 15°, 30°, 45°, 60°, 75°, and 90°. The specimen numbering system used ‘C’ for conventional bending tests, 0 for non-fractured specimens, and numbers like 15, 30, . . ., 90 for fracture angles, with 1, 2, and 3 indicating test replicates. For instance, ‘C-1’ denotes the first test of the conventional bending test. Similarly, ‘0–1’ represents the first test of the bending test on a non-fractured specimen, ‘15–2’ refers to the second test on a specimen with 15° prefabricated fractures.

2.2. Experimental system

As shown in Fig. 3a–e, the multi-angled prefabricated fracture specimen tensile fracture experiment under stepped loading stress levels encompasses both the loading phase and the 3D scanning procedure. Initially, the specimen was positioned on the four-point bending rams of the MTS 809.10 electro-hydraulic servo-sensile-torsion fatigue testing machine. The upper rams were spaced 80 mm apart, each 40 mm from the midpoint of the specimen, while the lower rams were symmetrically positioned with a 160 mm separation. After the specimen was fractured, a CRONOS 3D scanner was used to conduct a meticulous scan of the fracture surface. With a scanning resolution of up to 20 μm, it can scan the 3D morphology data of the fracture surface and acquire high-precision point cloud data. With a scanning accuracy of up to 20 μm, it could capture 3D morphological data and high-precision point cloud data of the fracture surface. Considering the small fracture surface size and complex undulation, the highest scanning resolution (20 μm) was selected. Subsequently, a 3D fracture surface model was constructed based on the scanning outcomes.

2.3. Stress path

(1) Conventional bending stress path: Before experimenting with Fig. 3a and b, conventional bending tests on non-fractured specimens were performed to measure their tensile strength. As illustrated in Fig. 3g, it represents the conventional bending stress path. In this study, three specimen groups, namely C-1, C-2, and C-3, were selected for the test. The test was performed at a loading rate of 4 N/s, following the loading stress path in Fig. 2e. The average peak load, F_{Max}, obtained from these experiments was used as the criterion for determining the stable stepped loading stress levels.

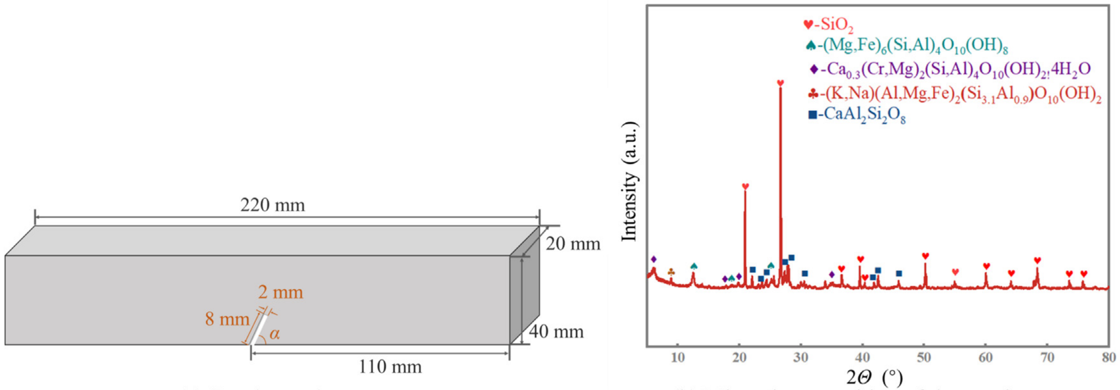

(a) Specimen size (b) Mineral composition of the specimen

Fig. 2. Specimen size and mineral composition.

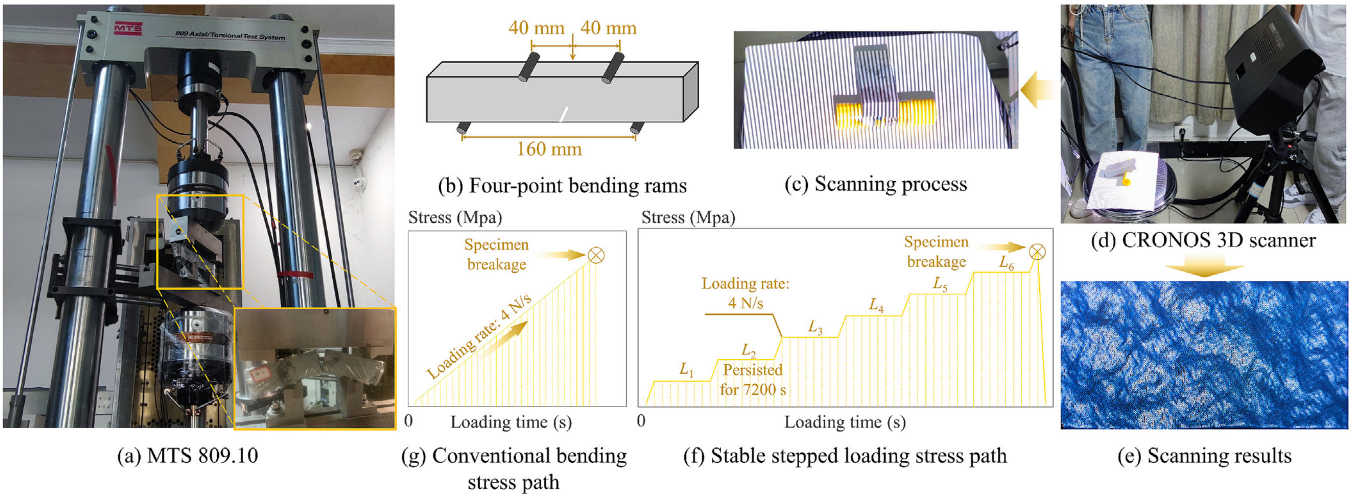

(a) MTS 809.10 (b) Four-point bending rams (c) Scanning process (d) CRONOS 3D scanner (e) Scanning results (f) Stable stepped loading stress path (g) Conventional bending stress path

Fig. 3. Experimental process.

(2) Stable stepped loading stress path: As shown in Fig. 3f, the stable stepped loading stress path incorporates multiple stress levels. Specifically, the stress level in the first stage was L_1=0.2 F_{Max}; in the second stage, L_2=0.4 F_{Max}; in the third stage, L_3=0.6 F_{Max}; in the fourth stage, L_4=0.8 F_{Max}; in the fifth stage, L_5=F_{Max}; and in the sixth stage, L_6=1.2 F_{Max}, and this pattern continued. Each stage lasted 7200 s. After each stage, the loading system would increase the stress level to the next stage at a rate of 4 N/s, continuing until specimen failure.

The F_{Max} values obtained from the conventional bending test, along with the stress levels at various stages of the stepped loading process, are listed in Table 1.

3. Characterization of fracture surface undulation response to initial fracture angle

In this section, the morphology of the fracture channels in the rock specimens is extracted after they undergo a tensile test, as shown in Fig. 4. Each fracture channel has two surfaces (Fig. 4a). Thus, it is essential to mark the names of the different surfaces of these fracture channels.

As shown in Fig. 4, in the non-fractured specimen, two fracture channels emerged within the specimen during tensile failure. When an initial fracture existed, the specimen formed only one fracture, which predominantly propagated from the tip of the initial fracture. By using the point-cloud data obtained from the CRONOS 3D high-precision scanner, the positional information of the scanned points on the fracture surface was extracted using MATLAB. Subsequently, 3D coordinate points were established, and the 3D spatial morphology of the surface was mapped, as shown in Fig. 5. In Fig. 5, (I) shows the 2D profile in the middle of the fracture surface; (II) shows its 3D morphology; and (III) shows the 2D contour map.

The fracture surface undulations are shown in Fig. 5. By comparing the undulation patterns at different initial fracture angles, it was evident that the areas with significant undulation were predominantly concentrated in the central portion of the fracture surface. Moreover, as the initial fracture angle increased, the height of the undulation on the fracture surface gradually migrated from the central region to the boundary. As manifested in Fig. 5a–f, from the non-fractured state to an initial fracture angle of 30°, the variation in the undulation height of the fracture surface of the specimen was the most remarkable. Meanwhile, the proportion of the highly undulating area on the surface was substantial. In Fig. 5g–n, for an initial fracture angle range of 45°–90°, the integrity of the fracture surface of the specimen after tensile failure was relatively high. The variation in the undulation height of the surface was minimal, and the proportion of the low-undulation areas was large. To effectively quantify and characterize the undulation patterns of the surface, in this section, by utilizing the 3D spatial coordinate information of the high-precision scanned points on the fracture surface, the maximum undulation height (based on peak-to-valley distance), average undulation height, and average undulation variance for each fracture surface were calculated (Table 2). Subsequently, the average values for the fracture surfaces at each initial fracture angle were computed, and the variation curves were plotted, as shown in Fig. 6.

Based on the undulation degree data in Table 2 and the variation patterns in Fig. 6, the maximum undulation height of the fracture surface reflects the size of the undulation range. The average undulation height indicates the global height of the fracture surface, and the average undulation variance represents the global undulation. A larger variance implies a greater average deviation from the mean, indicating a more dispersed distribution and more dramatic fluctuations. Smaller values of variance indicate that the data are closer to the average value. A larger variance indicates more significant undulation height changes, while a smaller one suggests gentler undulation changes. When the initial fracture

Table 1
The F_{Max} value and the stress levels at various stages.

Specimen No.	Peak load (N)	Average load F_{Max} (N)	Stress level	Loading value (N)	Stress level	Loading value (N)
C-1	1210	1196	L_1	239	L_4	957
C-2	1192		L_2	478	L_5	1196
C-3	1187		L_3	718	L_6	1434

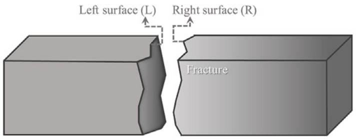

(a) Fracture surface naming

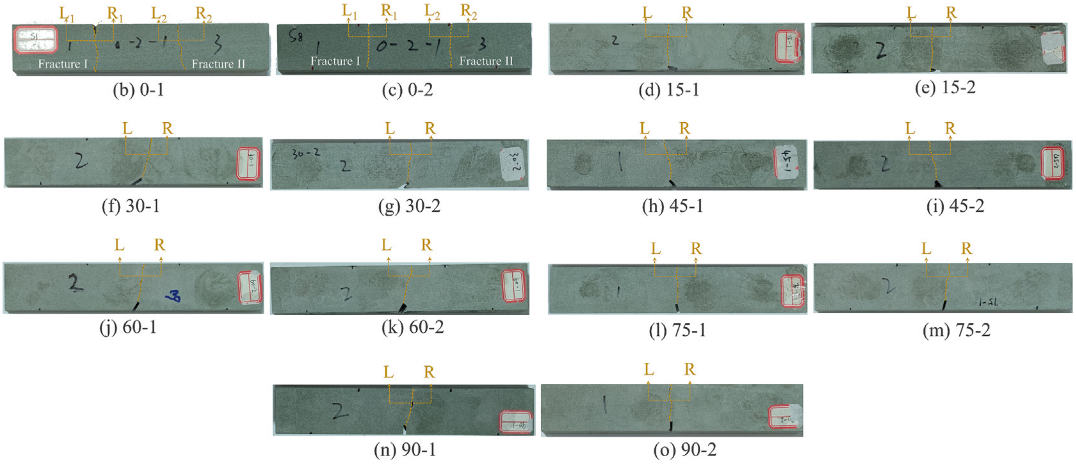

(b) 0-1 (c) 0-2 (d) 15-1 (e) 15-2
(f) 30-1 (g) 30-2 (h) 45-1 (i) 45-2
(j) 60-1 (k) 60-2 (l) 75-1 (m) 75-2
(n) 90-1 (o) 90-2

Fig. 4. Fracture morphology of specimens.

angle was 30°, the maximum undulation height, average undulation height, and average undulation of the fracture surface reached their highest values of 3.80 mm, 1.99 mm, and 0.30, respectively, which indicates that the fracture surface was very rough at an initial fracture angle of 30°. However, at an initial fracture angle of 75°, these values reached their lowest points: 2.40 mm, 1.19 mm, and 0.14, respectively, suggesting that the fracture surface was relatively smooth.

Furthermore, according to the undulation patterns of the fracture surface at different initial fracture angles, 45° was defined as the dividing angle. Initial fracture angles less than 45° fell into the high undulation range, while those greater than 45° were in the low undulation range. For the high undulation range, tensile testing revealed significant undulation on the fracture surface and high overall dispersion of changes. The fracture surface was not uniformly highly undulating; instead, local variations led to relatively high overall surface roughness. In the low undulation range, after the specimen underwent tensile testing, the undulation on the fracture surface was less pronounced. The undulation varied uniformly across the fracture surface, facilitating the formation of a smoother fracture surface.

4. Mechanism of gas flow guided by fracture surface undulation

4.1. The evolution law of the relative undulation degree and the stability

The gas flow on the fracture surface is significantly affected by the undulation of the fracture surface during the flow. If there is a high degree of undulation in the flow channel, the gas flow path in the fracture channel will be longer. Therefore, it is urgent to determine how the gas flow channels undulate on the fracture surface.

In Section 3, only the undulation patterns of the fracture surface under diverse initial fracture angles are elucidated. However, the extent of undulation within the fracture channels during gas flow remains unclear. To address this, as shown in Fig. 7, the 2D profiles of the gas flow channels were extracted at 5 mm intervals along the gas flow direction and plotted, as presented in Fig. 8.

According to the 2D profiles of the fracture surface extracted at different positions, as illustrated in Fig. 8, it becomes evident that the fracture surface traversed by the gas flow exhibits an undulating and non-uniform topography. When the initial fracture angle was less than 45°, the 2D profile of the fracture surface exhibited substantial undulation variations, characterized by conspicuous height differentials. Conversely, when the initial fracture angle exceeded 45°, the undulation changes of the 2D profile of the fracture surface were relatively gentle and devoid of drastic undulation fluctuations.

Meanwhile, although the 2D profiles at different positions (5, 10, and 15 mm) on the same fracture surface exhibited similar undulation trends, disparities exist among these profiles, implying that even within the same fracture surface, the gas flow characteristics at different locations are likely to differ. To characterize the influence exerted by the differences in undulation at various positions on the fracture surface during gas flow, the undulation variance of each 2D profile curve was computed to clarify the degree of undulation at distinct positions on the fracture surface. The quantitative results are presented in Table 3.

Based on Table 3, the undulation degree of different 2D profiles was clarified. Gas tends to flow through smoother pathways within the same fracture surface. However, when gas passes through different fracture surfaces, undulation during its passage is relative. It is challenging to compare the gas flow stability on fracture surfaces with different initial fracture angles solely based on the undulation variances of the profiles of different fracture surfaces. Take the 5 mm profiles of Surface 15-1 (L) and Surface 60-2 (R) as examples. The degrees of undulation of the two profiles were similar (0.20 and 0.18, respectively). However, the undulation degree varied within the respective surfaces. At the 5 mm position of Surface 15-1 (L), the undulation variance was at a minimum, whereas at the 5 mm position of Surface 60-2 (R), the undulation variance was remained higher than that at the 10 mm position on the same surface. Therefore, this method of quantifying the undulation degree can only determine the impact exerted by the overall undulation of the fracture surface. However, it is challenging to reflect the stability in the gas flow process, which is induced by the

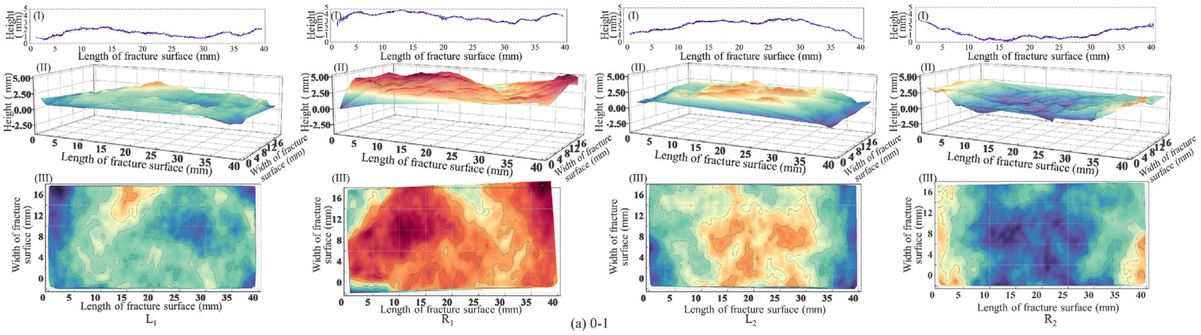

(a) 0-1

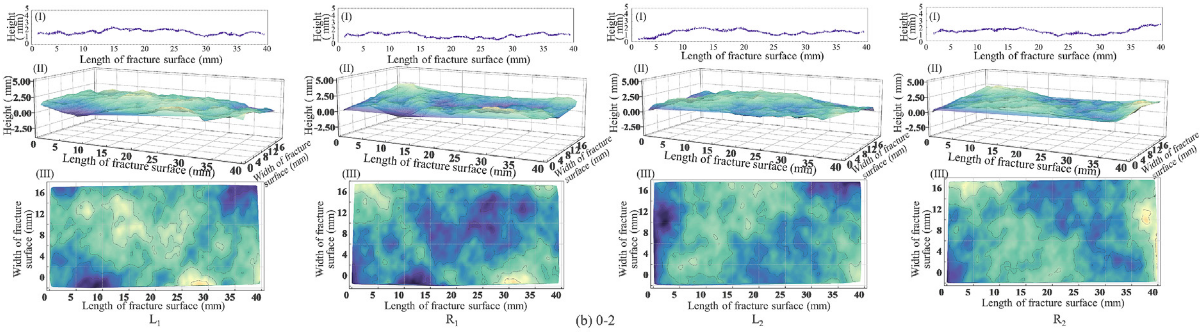

(b) 0-2

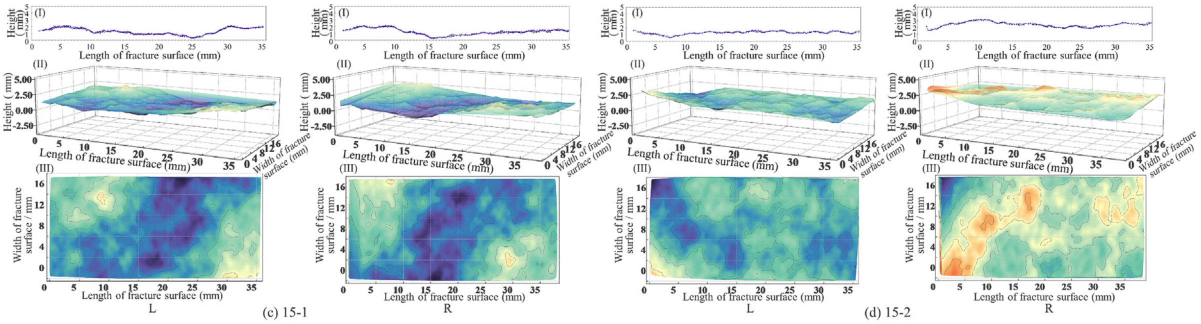

(c) 15-1 (d) 15-2

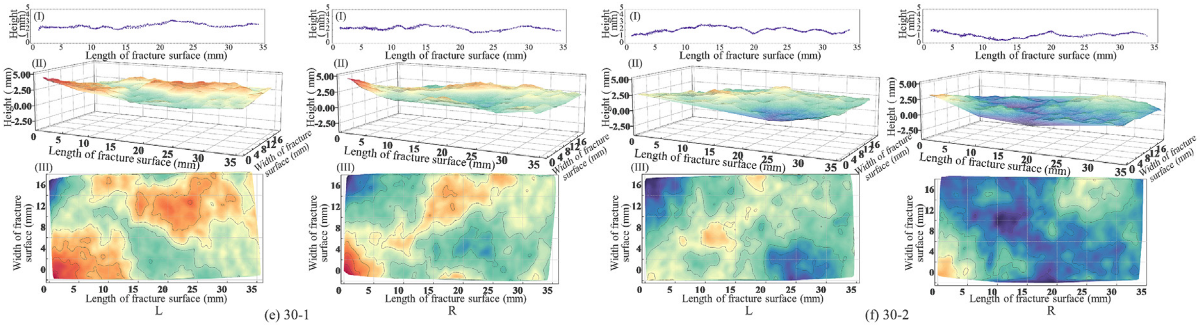

(e) 30-1 (f) 30-2

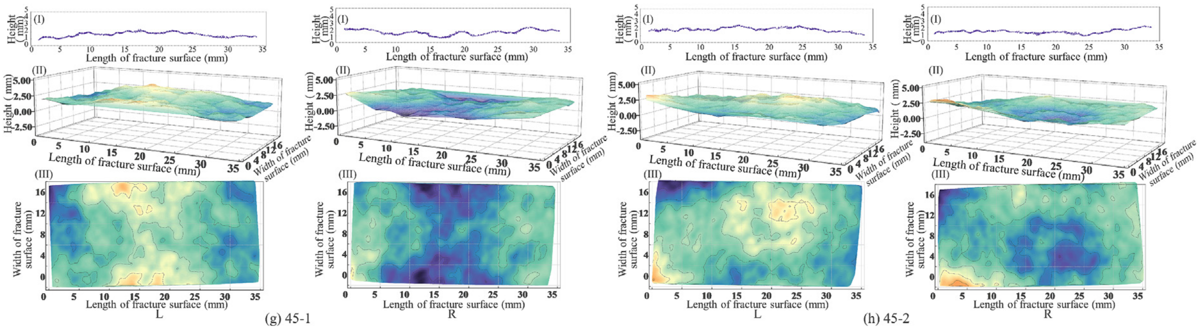

(g) 45-1 (h) 45-2

Fig. 5. 3D morphology of the fracture surfaces.

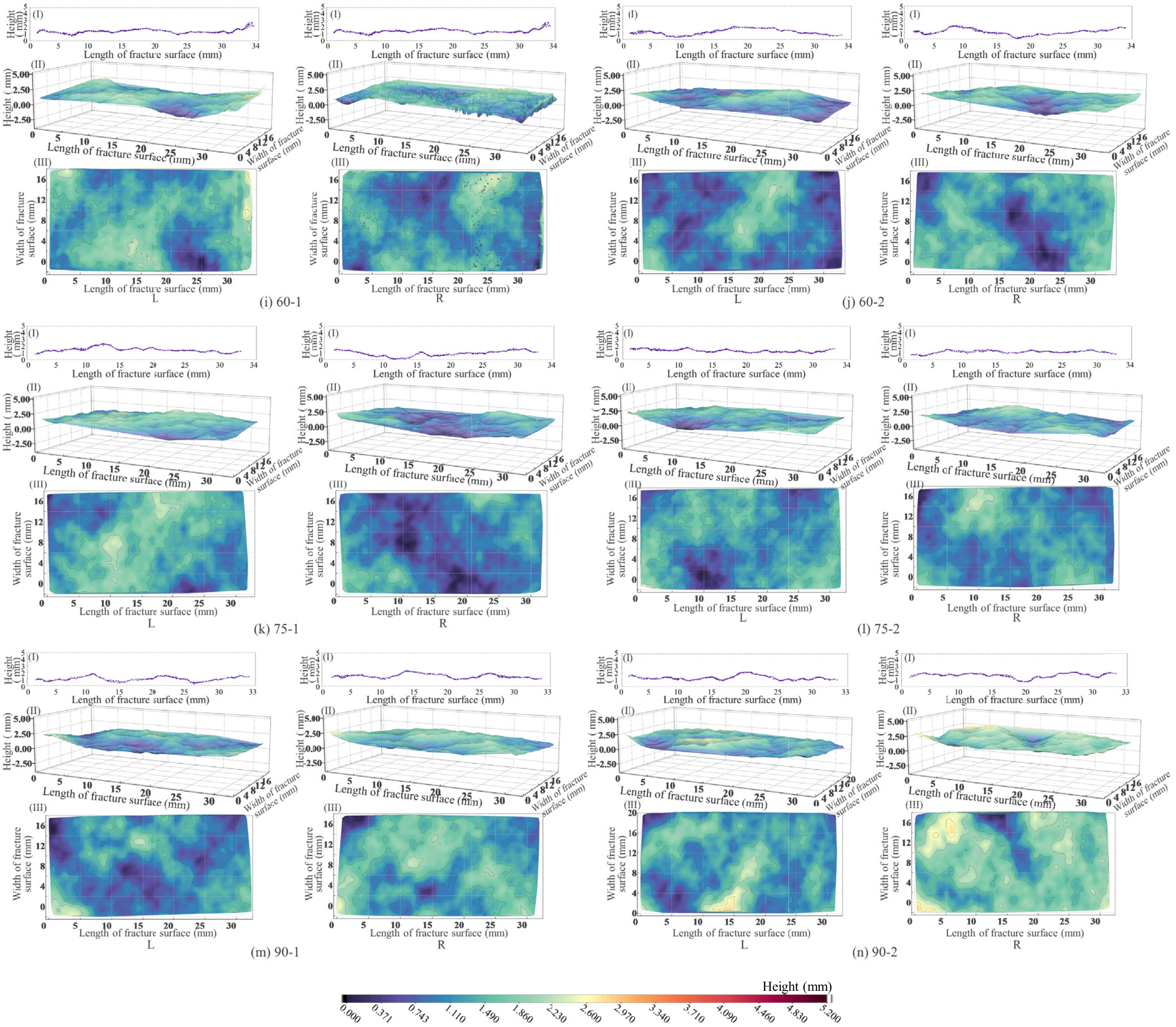
(i) 60-1 (j) 60-2 (k) 75-1 (l) 75-2 (m) 90-1 (n) 90-2

Fig. 5 (*continued*)

Table 2
Undulation values of each fracture surface.

Surface name	Maximum undulation height (mm)	Average undulation height (mm)	Average undulation variance	Surface name	Maximum undulation height (mm)	Average undulation height (mm)	Average undulation variance
0–1 (L_1)	3.25	1.71	0.27	45–1 (L)	3.04	1.79	0.24
0–1 (R_1)	5.21	3.56	0.43	45–1 (R)	2.69	1.30	0.23
0–1 (L_2)	3.49	2.30	0.43	45–2 (L)	3.14	1.80	0.24
0–1 (R_2)	3.39	1.38	0.44	45–2 (R)	3.24	1.51	0.22
0–2 (L_1)	2.83	1.61	0.19	60–1 (L)	3.02	1.40	0.16
0–2 (R_1)	2.82	1.25	0.18	60–1 (R)	3.02	1.40	0.15
0–2 (L_2)	2.36	2.36	0.16	60–2 (L)	2.26	1.04	0.19
0–2 (R_2)	2.82	1.46	0.16	60–2 (R)	2.13	1.25	0.18
15–1 (L)	2.80	1.32	0.31	75–1 (L)	2.38	1.41	0.15
15–1 (R)	2.81	1.33	0.31	75–1 (R)	2.32	0.95	0.15
15–2 (L)	2.96	1.46	0.14	75–2 (L)	2.55	1.23	0.13
15–2 (R)	3.77	2.23	0.20	75–2 (R)	2.36	1.20	0.13
30–1 (L)	4.53	2.58	0.31	90–1 (L)	2.51	1.08	0.15
30–1 (R)	4.52	2.18	0.30	90–1 (R)	2.53	1.42	0.15
30–2 (L)	3.09	1.88	0.28	90–2 (L)	2.82	1.33	0.17
30–2 (R)	3.09	1.33	0.28	90–2 (R)	2.98	1.73	0.18

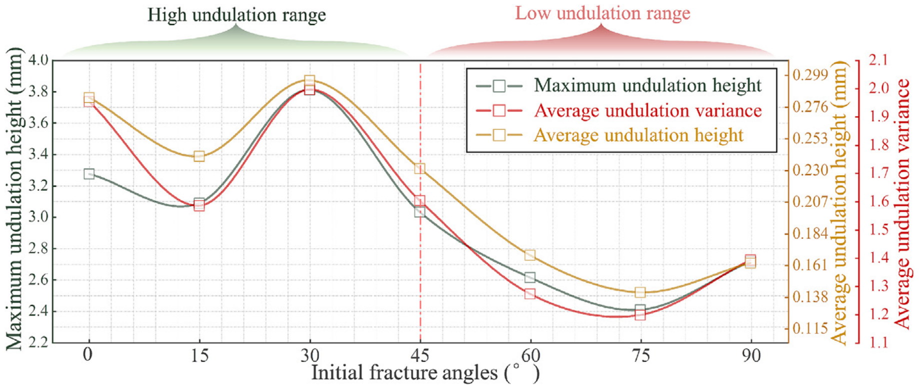

Fig. 6. The undulation variation pattern of the fracture surface.

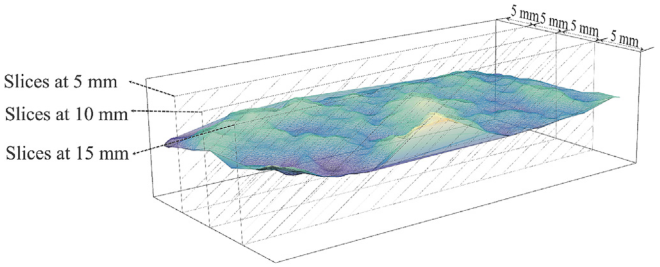

Fig. 7. 2D profile extraction from fracture surfaces.

variances in undulation height changes at different positions within the fracture surface. Consequently, to eliminate the influence of the global undulation of diverse fracture surfaces on the determination of gas flow at different positions on the fracture surface, this section uses the relative undulation degree for quantitative characterization, as illustrated in Eqs. (1) and (2).

$$V_{\mathrm{cr}} = \frac{V_{cd} - \min(V_c)}{\max(V_c)} \tag{1}$$

$$V_c = [V_{c5}, \cdots V_{cd}] \tag{2}$$

where V_{cr} stands for the relative undulation degree of different fracture surfaces, $V_{\mathrm{cr}} \in [0,1]$, the closer to 1 indicates that the relative undulation degree is larger; V_{cd} the undulation degree at different locations of the fracture surfaces; V_c the set of undulation intensities at different fracture surfaces; and c is for different fracture surfaces, c = 0–1 (R_1), . . ., 90–2 (L); and d is for different locations, d = 5, 10, 15.

The variance of undulation at 5, 10, and 15 mm on the fracture surface is calculated and stored in array V_c. Then, normalization methods are utilized to calculate the relative undulation V_{cr}. The variation in relative undulation of fracture surfaces characterizes the effect of undulation height variability on gas flow stability at different positions within fractures. A larger relative undulation indicates significant local undulation, leading to weaker gas flow stability, and vice versa. Meanwhile, this undulation degree quantification method effectively eliminates the influence of inter-fracture undulation differences in comparing gas flow stability across fractures, enabling valid comparisons of undulation characteristics between different fracture surfaces. The changes in the relative undulation degree of the rock fracture surface can be utilized to represent the stability in the gas flow process, which is engendered by the differences in undulation height changes at various positions within the fracture surface. Additionally, the established method of quantifying undulation degree can effectively mitigate the impact the global undulation on different fracture surfaces on determining gas flow stability. The relative undulation degree quantifies the extent of undulation variations in channels at various positions within a fracture surface compared to those at other locations on the same fracture surface. Moreover, it enables in-depth analysis and comparison of the flow stability of the gas as it flows through the fracture surfaces under the influence of different initial fracture angles, considering the computational outcomes derived from Eqs. (1) and (2), illustrate the relative undulation degree at different positions across various fracture surfaces, as graphically represented in Fig. 9.

Fig. 9 shows the relative undulation degree of the fracture surfaces. Based on the relative undulation degree distribution, the evolution of the fracture surface was partitioned into three intervals. In the non-fractured specimen, demarcating Interval I, only one side of the different fracture surfaces showed slight undulation, mainly at the surface edge. Consequently, within this interval, the gas flows more smoothly at the fracture surface edge than at other locations, demonstrating a stability in flow within this area. When the initial fracture angle ranged from 15° to 45°, the middle position of the fracture surface was relatively smooth, while both sides had significant undulation, thus defining Interval II. Within this interval, the gas stable flows through the middle pathway of the fracture surface. When the initial fracture angle ranged between 60° and 90°, the smooth area of the fracture surface enlarged, which was identified as Interval III. Consequently, the range within which gas can flow smoothly in this interval is extensive.

4.2. Characteristics of the relative undulation frequency and the tortuosity

In Sections 3 and 4.1, investigations and analysis were conducted on the 3D morphology of the fracture surface and the undulation degree of the fracture channels, respectively. Building upon these research outcomes, this section presents a statistical analysis of the frequencies of diverse undulation heights on the fracture surfaces. Here, in this section, the maximum undulation range of the fracture surface, spanning from 0 to 4.60 mm, is considered the maximum partition interval for the undulation frequencies. A statistical interval for undulation height was established at intervals of 0.2 mm, culminating in a total of 23 undulation height intervals. Subsequently, the proportion of each undulation height interval within the fracture surface was calculated. The undulation frequency equation is presented in Eq. (3). First, the number of measuring points within different undulation height intervals of the fracture surface is counted. Next, the frequency of each undulation height interval is derived by

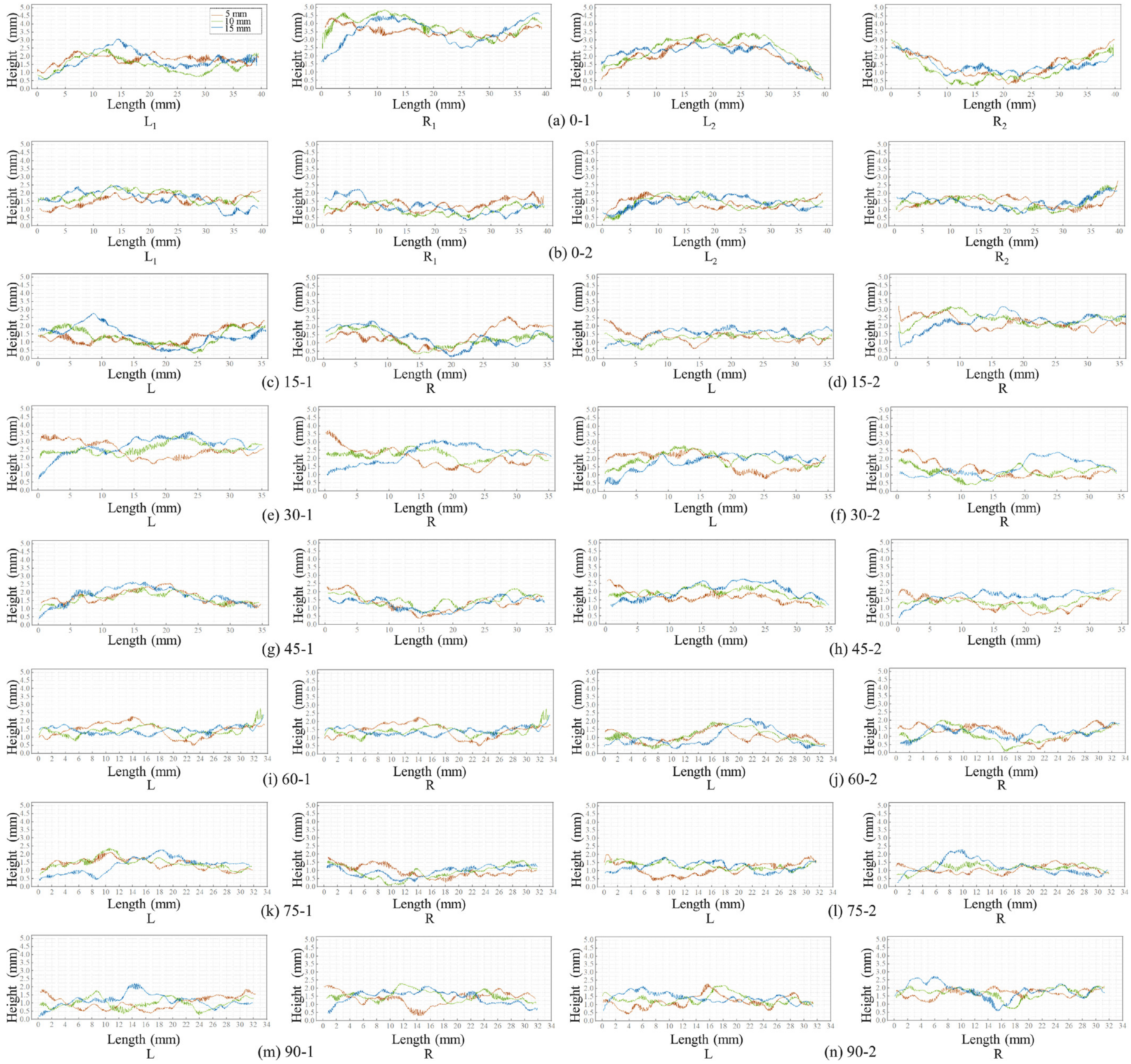

(a) 0-1 (b) 0-2 (c) 15-1 (d) 15-2 (e) 30-1 (f) 30-2 (g) 45-1 (h) 45-2 (i) 60-1 (j) 60-2 (k) 75-1 (l) 75-2 (m) 90-1 (n) 90-2

Fig. 8. 2D profiles of fracture surface at different locations.

dividing the number of measuring points in each interval by the total number of measuring points on the fracture surface. The statistical results of the undulation height change frequencies of the fracture surfaces of each specimen are shown in Fig. 10.

$$R_{\mathrm{fn}} = \frac{R_{\mathrm{n}}}{N_{\mathrm{T}}} \times 100\% \tag{3}$$

where R_{fn} is the relative frequency of different undulation height intervals, %; R_{n} the number of measuring points in different undulation height intervals; and N_{T} the number of all measurement points on the fracture surface.

As shown in the statistical outcomes of the fracture surface undulation height frequency in Fig. 10, fracture surfaces with different initial angles exhibit distinct undulation height distribution characteristics. Nevertheless, the overall variation pattern assumes a ‘single-peaked’ pattern. In the undulation height distribution interval of the fracture surface, the proportion of mid-range undulation heights is high, decreasing gradually when moving away from the mid-region. Moreover, the sharper the ‘peak’ of the fracture surface undulation height frequency, the more concentrated the range of undulation height variation on the fracture surface. However, in Fig. 10, only a qualitative assessment of the peak profile variation can be carried out. Specifically, the closer the initial fracture angle of the fracture surface is to 90°, the sharper the ‘peak’ becomes. Consequently, in this section, a methodology integrating the cumulative frequency of undulation height with the Boltzmann function fitting approach (Eq. (4)) is proposed. By calculating the slope of the fitting function, the aim was to quantitatively characterize the degree of concentration of the undulation on the fracture surface. When the slope of the fitting curve is larger, it indicates that the undulation height of an undulation interval position occurs within the fracture surface, and the undulation

Table 3
Quantification of 2D profile undulations.

Surface No.	Profile location (mm)	Profile undulation variance	Surface No.	Profile location (mm)	Profile undulation variance	Surface No.	Profile location (mm)	Profile undulation variance
0–1 (L_1)	5	0.07	15–2 (R)	5	0.14	60–2 (L)	5	0.11
	10	0.22		10	0.13		10	0.17
	15	0.31		15	0.19		15	0.28
0–1 (R_1)	5	0.10	30–1 (L)	5	0.24	60–2 (R)	5	0.18
	10	0.30		10	0.11		10	0.20
	15	0.53		15	0.35		15	0.10
0–1 (L_2)	5	0.45	30–1 (R)	5	0.34	75–1 (L)	5	0.10
	10	0.50		10	0.08		10	0.11
	15	0.20		15	0.31		15	0.23
0–1 (R_2)	5	0.46	30–2 (L)	5	0.26	75–1 (R)	5	0.12
	10	0.48		10	0.16		10	0.16
	15	0.21		15	0.28		15	0.09
0–2 (L_1)	5	0.10	30–2 (R)	5	0.26	75–2 (L)	5	0.14
	10	0.10		10	0.15		10	0.04
	15	0.22		15	0.26		15	0.08
0–2 (R_1)	5	0.10	45–1 (L)	5	0.16	75–2 (R)	5	0.06
	10	0.10		10	0.11		10	0.05
	15	0.21		15	0.27		15	0.19
0–2 (L_2)	5	0.10	45–1 (R)	5	0.26	90–1 (L)	5	0.16
	10	0.17		10	0.14		10	0.10
	15	0.14		15	0.12		15	0.14
0–2 (R_2)	5	0.09	45–2 (L)	5	0.12	90–1 (R)	5	0.14
	10	0.17		10	0.07		10	0.11
	15	0.13		15	0.22		15	0.17
15–1 (L)	5	0.20	45–2 (R)	5	0.17	90–2 (L)	5	0.16
	10	0.23		10	0.07		10	0.10
	15	0.38		15	0.12		15	0.08
15–1 (R)	5	0.32	60–1 (L)	5	0.19	90–2 (R)	5	0.05
	10	0.21		10	0.08		10	0.11
	15	0.32		15	0.05		15	0.22
15–2 (L)	5	0.10	60–1 (R)	5	0.19			
	10	0.04		10	0.08			
	15	0.11		15	0.05			

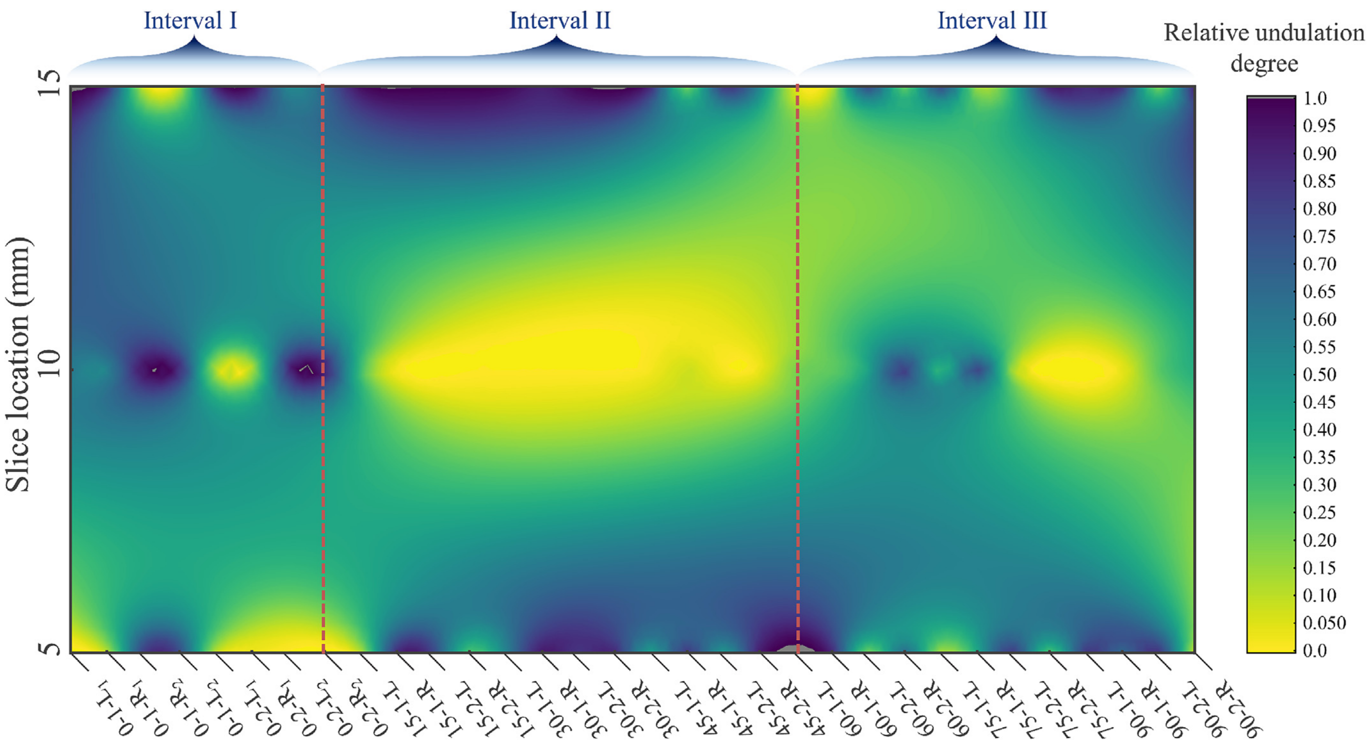

Fig. 9. Relative undulation degree for different fracture surfaces.

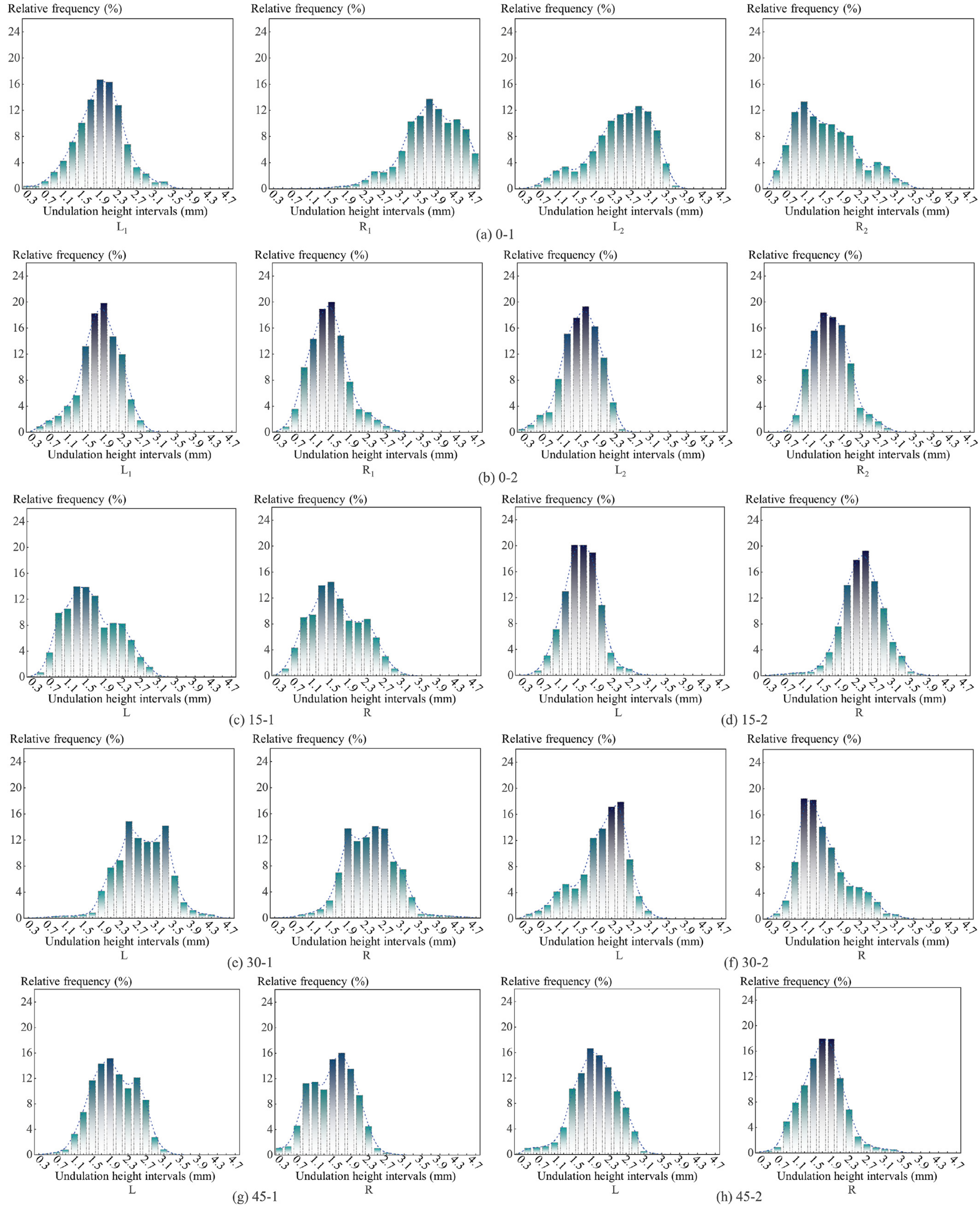

(a) 0-1

(b) 0-2

(c) 15-1

(d) 15-2

(e) 30-1

(f) 30-2

(g) 45-1

(h) 45-2

Fig. 10. Frequency of undulation height intervals.

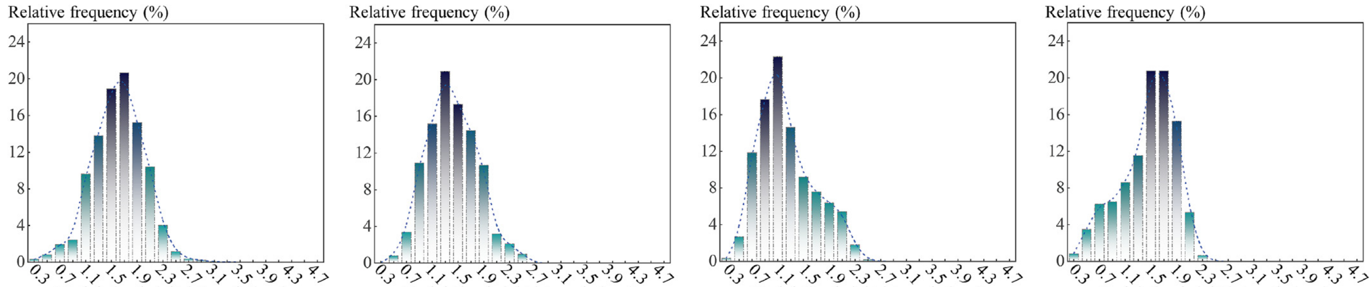

(i) 60-1 (j) 60-2

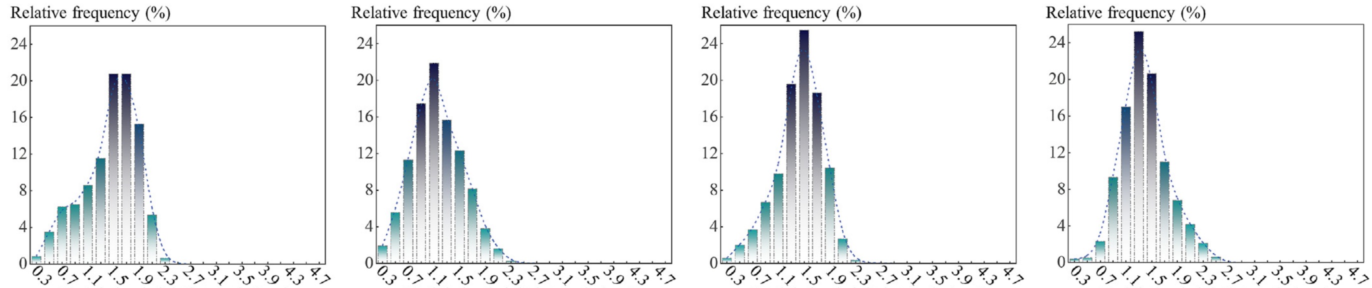

(k) 75-1 (l) 75-2

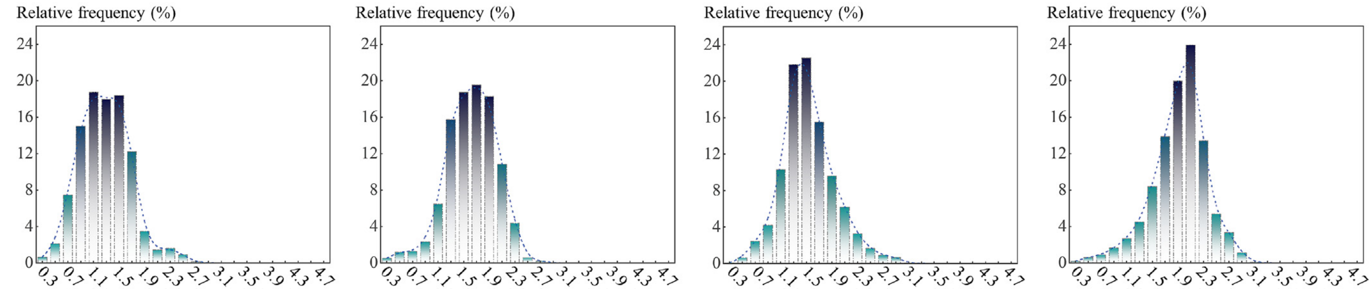

(m) 90-1 (n) 90-2

Fig. 10 (*continued*)

of the fracture surface changes; when the slope of the growth curve is smaller, it indicates that a variety of undulation heights exist within the fracture surface, and the gas flow path is more tortuous. The fitting curves are shown in Fig. 11. The parameters of the fitting function are listed in Table 4.

$$y = \frac{A_1 - A_2}{1 + e^{(x - x_0)/dx}} + A_2 \tag{4}$$

where y is the cumulative frequency, %; x the undulation interval, mm; and A_1, A_2, x_0, d_x the Boltzmann function fitting parameters.

Fig. 11 and Table 4 show the fitting parameters of the cumulative frequency of the fracture surface undulation. All the R^2 values of the fitting curves exceeded 0.99, indicating that the fitting results obtained by applying the Boltzmann function in this section were reliable. Moreover, the average slope of the fitting curve serves as an indicator of the degree of concentration of the undulations on the fracture surface. When the degree of concentration of the fracture surface undulation is high, there is a disparity in the proportion of an undulation interval compared with the others. Consequently, the cumulative proportion within this interval was substantial. Thus, the cumulative growth curve exhibits a rapid upward rise, i.e., the cumulative proportion increases sharply, resulting in a steeper curve with a larger slope. During gas flow in the fracture channel, the gas merely needs to surmount the undulation height change of a specific part of the fracture surface, resulting in low flow tortuosity. Conversely, if the fracture surface undulations are relatively scattered, meaning that different undulation intervals have a certain proportion and these proportions are similar. In that case, the cumulative growth curve exhibits a stable and smooth growth rate. The curve is gentle with a small slope. Gas flow traverses multiple undulation intervals, leading to higher tortuosity. When the size of each undulation interval is the same, the slope of the curve is exactly 1. The average slopes of the fracture surfaces corresponding to different initial fracture angles are listed in Table 4. In this section, the curves depicting their variations are plotted, as shown in Fig. 12.

The median value of the curved slopes (with a slope of 17.61) corresponding to different initial fracture angles was adopted as the reference line. As shown in Fig. 12, the variation patterns of the fitting curves were divided into undulation-concentrated and undulation-discrete intervals. Employing the median line to divide the undulation interval can effectively avert the impact of overly large or small slopes, which are caused by fracture surfaces with either highly concentrated or extensively dispersed undulations, on the dividing reference line. For initial angles of 15°–30° and 75°–90°, the slopes of the fitting curves were large, falling within the undulation concentrated segment. During the tensile process of the specimens, the fracture surfaces in these cases formed rapidly and were torn. Undulations mainly centered around a certain height are likely to occur on the fracture surface.

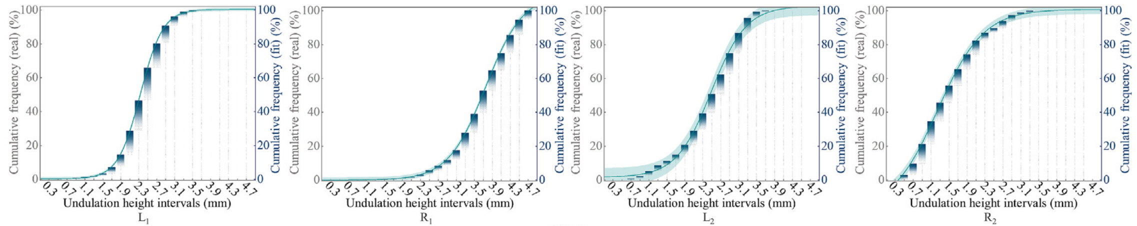

(a) 0-1

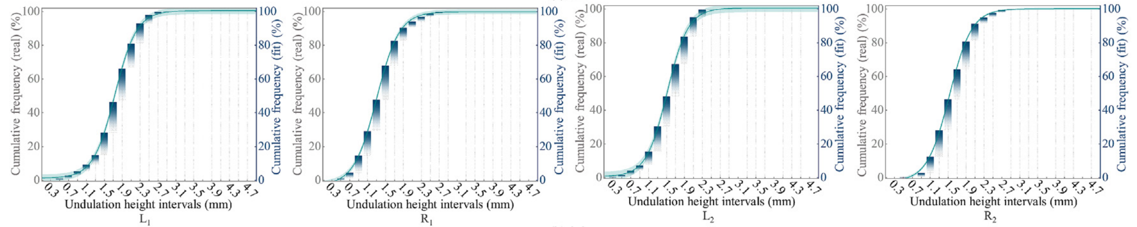

(b) 0-2

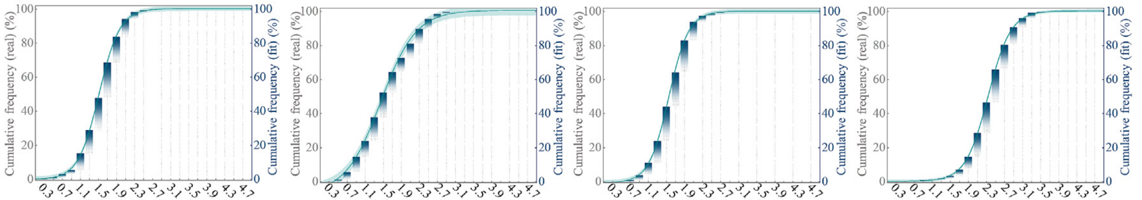

(c) 15-1 (d) 15-2

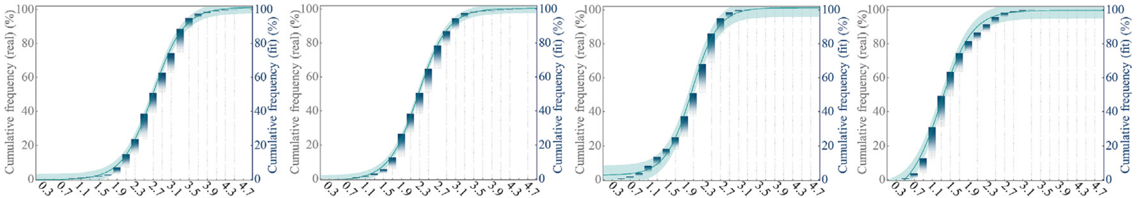

(e) 30-1 (f) 30-2

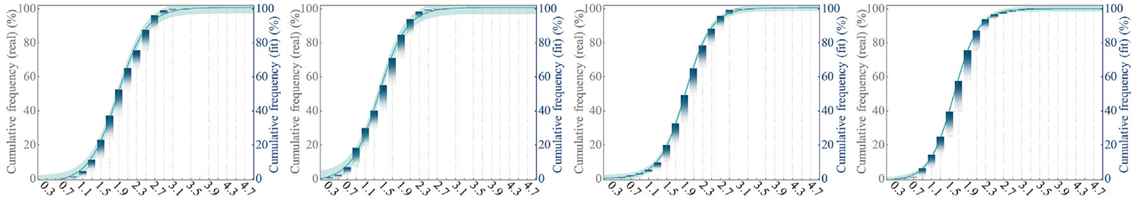

(g) 45-1 (h) 45-2

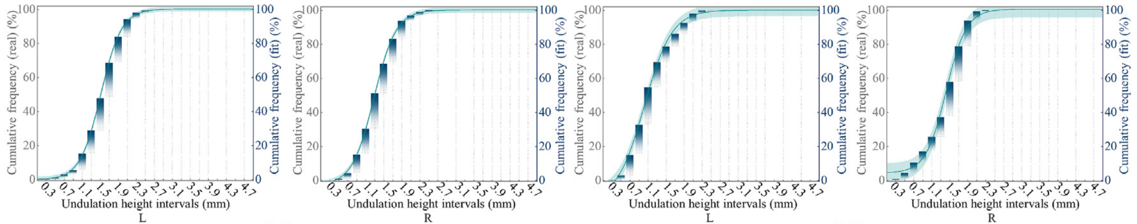

(i) 60-1 (j) 60-2

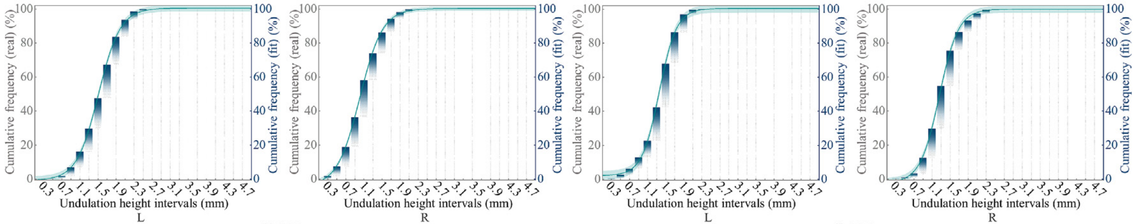

(k) 75-1 (l) 75-2

Fig. 11. Fitting analysis of fracture surface undulation cumulative frequency.

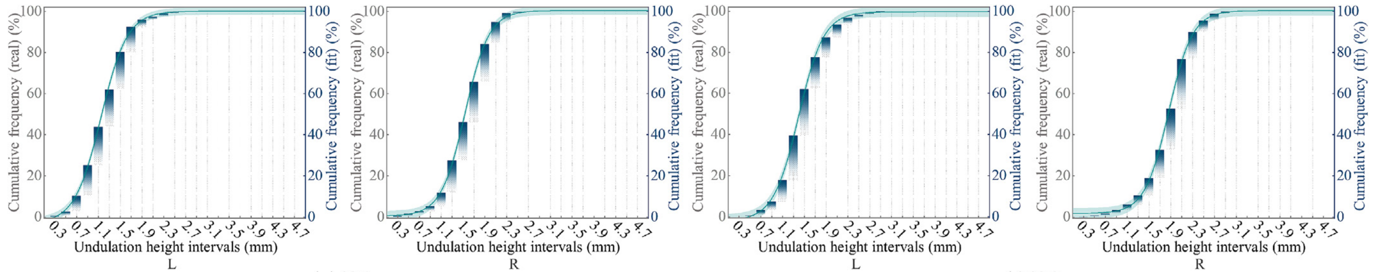

(m) 90-1 (n) 90-2

Fig. 11 (*continued*)

Table 4
Parameters of the fitting curves.

Initial fracture angle (°)	Surface No.	A_1	A_2	x_0	d_x	R^2	Slope of the curve	Average slope
0	0–1 (L_1)	0.18	100.22	8.58	1.46	0.99981	17.08	16.57
	0–1 (R_1)	−0.09	109.90	18.28	2.09	0.99961	13.18	
	0–1 (L_2)	1.55	102.65	11.96	1.95	0.99714	12.98	
	0–1 (R_2)	−17.92	100.74	5.75	2.54	0.99884	11.66	
	0–2 (L_1)	0.10	100.00	8.19	1.10	0.99955	22.70	
	0–2 (R_1)	−2.92	99.83	6.03	1.27	0.99970	13.18	
	0–2 (L_2)	0.60	100.47	7.09	1.17	0.99929	21.26	
	0–2 (R_2)	−2.39	100.02	7.16	1.25	0.99949	20.50	
15	15–1 (L)	−7.94	100.60	6.64	1.98	0.99858	13.73	17.61
	15–1 (R)	−6.72	100.64	6.73	1.95	0.99874	13.76	
	15–2 (L)	−0.64	100.16	7.27	1.10	0.99979	22.96	
	15–2 (R)	0.26	100.31	11.19	1.25	0.99992	19.98	
30	30–1 (L)	−0.33	101.19	13.00	1.69	0.99879	15.03	15.82
	30–1 (R)	−0.86	100.34	10.87	1.63	0.99917	15.48	
	30–2 (L)	2.72	101.18	9.83	1.45	0.99677	16.96	
	30–2 (R)	−9.34	99.62	5.97	1.72	0.99653	15.82	
45	45–1 (L)	−1.95	100.74	8.89	1.60	0.99864	16.09	17.23
	45–1 (R)	−1.22	100.72	6.51	1.53	0.99782	16.63	
	45–2 (L)	0.29	100.55	9.10	1.43	0.99961	17.49	
	45–2 (R)	−0.92	100.05	7.50	1.35	0.99973	18.71	
60	60–1 (L)	−0.03	100.25	7.08	1.16	0.99976	21.69	20.57
	60–1 (R)	−2.88	100.17	5.93	1.23	0.99962	20.99	
	60–2 (L)	−12.16	100.08	4.60	1.53	0.99763	18.32	
	60–2 (R)	4.34	100.62	6.61	1.13	0.99653	21.29	
75	75–1 (L)	−0.67	100.42	7.07	1.21	0.99955	20.89	21.62
	75–1 (R)	−4.14	100.18	4.57	1.26	0.99970	20.78	
	75–2 (L)	−4.14	100.18	4.57	1.26	0.99923	20.78	
	75–2 (R)	−2.14	99.83	5.82	1.06	0.99940	24.03	
90	90–1 (L)	−2.95	100.08	5.25	1.21	0.99947	21.30	22.10
	90–1 (R)	0.54	100.36	7.20	1.10	0.99946	22.65	
	90–2 (L)	−1.85	99.65	6.49	1.16	0.99916	21.95	
	90–2 (R)	1.74	100.33	8.82	1.10	0.99990	22.50	

During the gas flow process, the gas mainly flows through this undulation height, resulting in a relatively low tortuosity of the gas flow. Conversely, in the cases of non-fractured specimens and initial fracture angles in the interval from 45° to 60°, the slopes of the fitting curves were small and were located within the undulation-discrete interval. The specimens took a relatively long time to exhibit significant deformation before fracturing. Thus, the uniformity of each undulation interval on the fracture surface was high. Gas flow traverses multiple intervals, leading to high tortuosity.

4.3. Law of gas flow response to meshing degree

4.3.1. Numerical modelling of fracture channels

Based on the research in Sections 4.1 and 4.2, this section constructed numerical models of the gas flow channel. The gas flow process was simulated using COMSOL. Fig. 13 shows the construction process of the numerical model for gas flow on the fracture surface. As can be seen from the extraction results of the fractures in the specimen after failure in Fig. 4, the fracture channel is composed of a combination of the R and L surfaces. Therefore, the 3D morphology models of the R and L surfaces were combined to form the channel model. One end of the model was set as the inlet, the other end as the outlet, and the remaining boundaries as the walls. The numerical model is established based on the Navier-Stokes equations [28], with the governing equation in COMSOL specified as Eq. (1). This study focuses on the long-term spontaneous steady-state gas flow in rock fractures after coal seam mining ceases. Simultaneously, the conditions of gas deposition in different mines vary, and thus, the residual gas content of the working face also differs. In the goaf, the range of diffusion flow of gas is influenced by the residual gas content [5,29]. Considering the

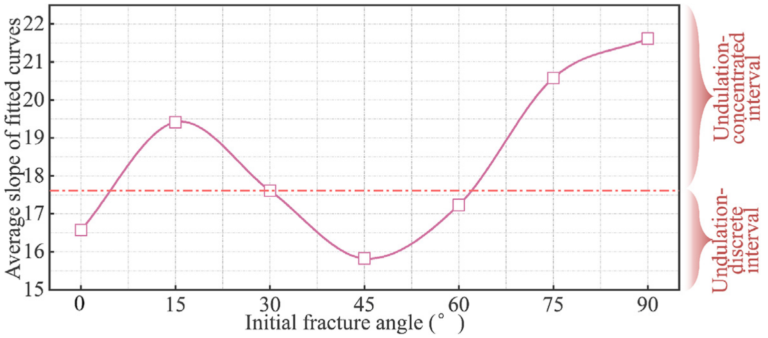

Fig. 12. Average slopes of fitted curves for different initial fracture angles.

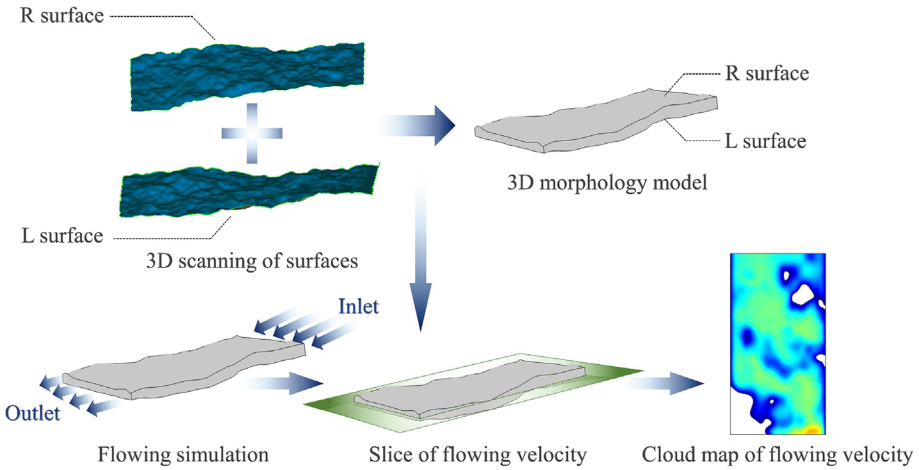

Fig. 13. Numerical modeling of gas flow in fracture channels.

steady-state flow conditions in this study, a low-flow inlet boundary condition (1×10^{-6} m^3/s) is imposed, while the outlet boundary is set to 0 Pa.

$$\rho(u\cdot\nabla)u=\nabla\cdot(-P\mathrm{I}+K)+F \tag{5}$$

where P is the pressure, Pa; ρ the density of gas, kg/m^3; u the velocity of gas, m/s; I the unit second-order tensor; K the viscous stress tensor, Pa; and F the external fore per unit volume, N.

Finally, a velocity-slice cloud map of the channel was constructed to analyze the gas flow process. This numerical simulation method was developed based on the real 3D morphology model of the fracture surface, accurately reflecting the influence of fracture surface undulation on gas flow.

4.3.2. Evolution law of gas flow in fracture channels

From the numerical simulation results, gas flow behaviors in the fracture channels with different initial fracture angles were determined. As illustrated in Fig. 14, velocity cloud map slices at different positions within the fracture channels were generated to analyze gas flow variations in the fracture channels.

Based on the numerical simulation results, the gas flow stability and tortuosity indexes proposed in Sections 4.1 and 4.2 are herein further validated.

(1) Validation of gas flow stability

Flow stability is defined as the uniformity of gas flow variation within fracture surfaces. Fig. 14 illustrates velocity change contour slices of each fracture channel. Furthermore, the measuring lines were set at 2 mm intervals along the y-direction of each numerical model and the variances of the velocity change on these lines are calculated and plotted in Fig. 15a. According to Fig. 15b and c, the variance of the velocity change at a certain position on the fracture surface is lower than at other positions in the fracture channel of the non-fracture specimens, indicating uniform gas flow. For the initial fracture angle of 15°–45° (Fig. 15d–f), the variance curves at different fracture surface positions exhibit a roughly 'V' shape, showing that gas flow is more uniform near the surface midpoint. Therefore, the gas flow at the middle position is less disturbed, with minimal velocity fluctuations. When initial fracture angles are 60°–90° (Fig. 15h and i), variance change curves reveal two regions of low variance at different surface positions, indicating a larger uniform flow area. Combined with Section 4.1, the change in the undulation of the fracture surface for different initial fracture angles is categorized into three intervals, with one-sided smoothing in Interval I, intermediate smoothing in Interval II, and bilateral smoothing in Interval III. The small variation in gas flow velocity in the smooth region indicates a uniform flow process, which validates the flow stability discussed in Section 4.1.

(2) Validation of gas flow tortuosity

The pressure cloud maps of the fracture surface are shown in Fig. 16. The high-pressure region on the fracture surface is concentrated at the inlet, while the low-pressure region lies at the outlet. To quantitatively assess the impact of different initial fracture angles on the pressure of the fracture surface, the mean values of the maximum pressure corresponding to various initial fracture

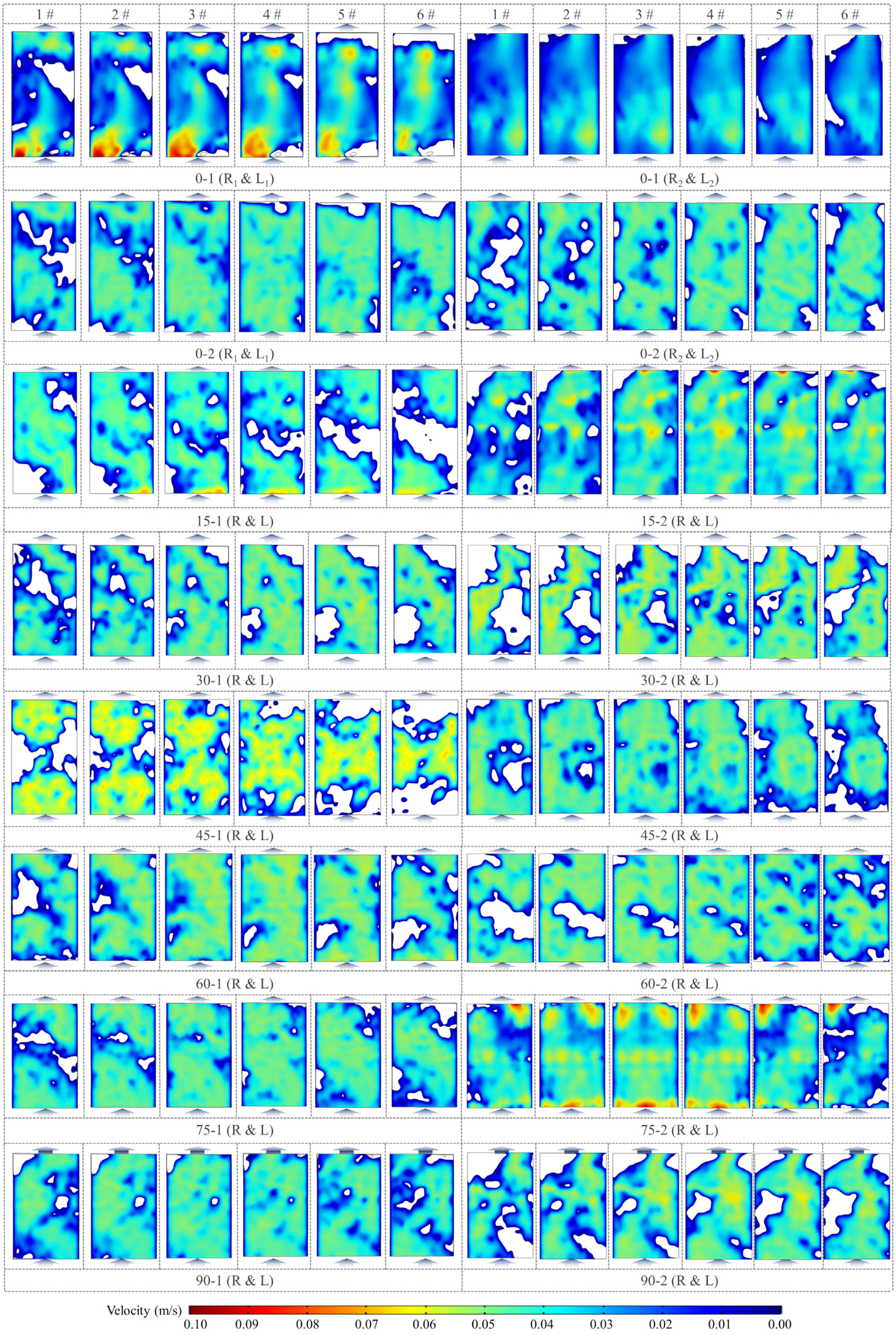

Fig. 14. Slices of the gas flow velocity cloud map.

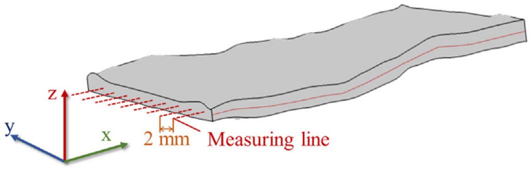

(a) The positions of measuring line

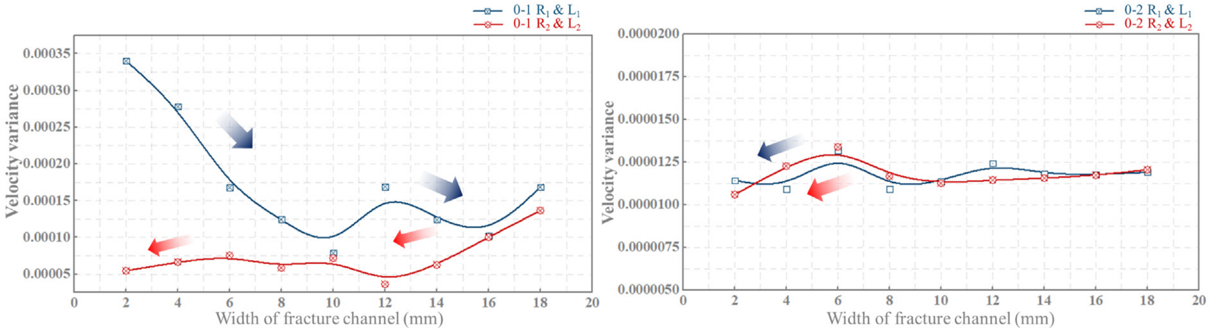

(b) 0-1 (c) 0-2

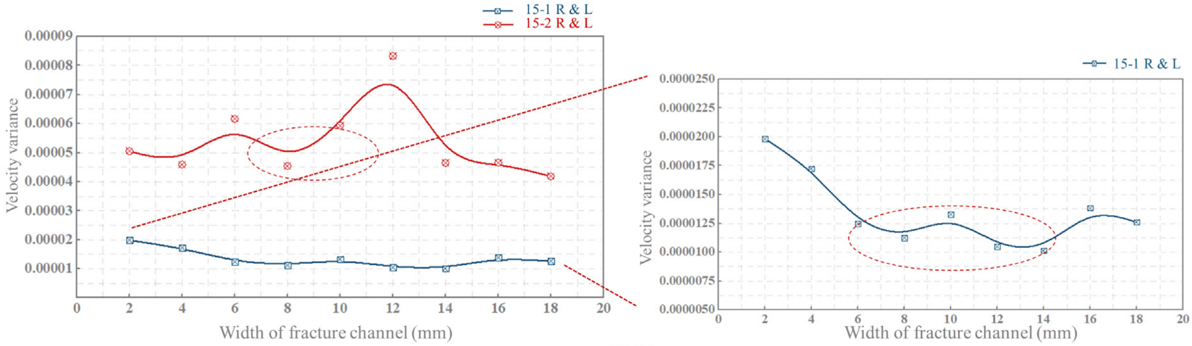

(d) 15

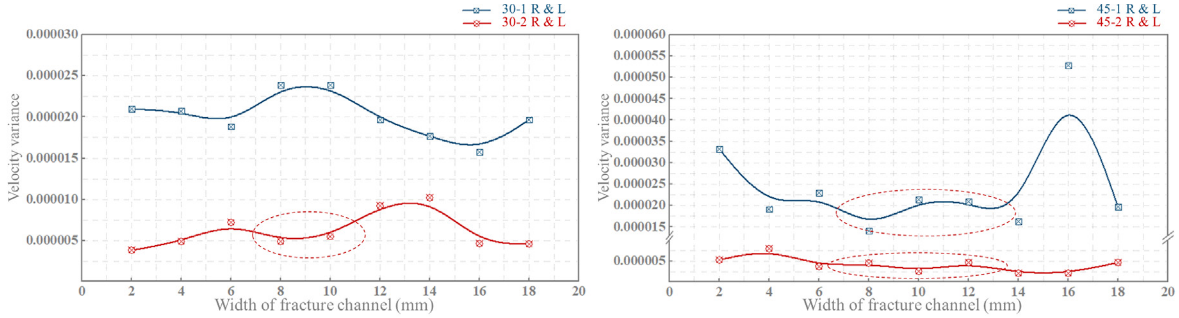

(e) 30 (f) 45

Fig. 15. Velocity variance at different positions.

angles were extracted from the fracture surface. Subsequently, the pressure values were normalized using Eq. (6). The normalization method normalizes wall pressure, enabling simulation results to focus on pressure variation patterns and enhancing the universality of study conclusions. Additionally, Fig. 17 shows the curve of the mean maximum pressure values in the fracture channels. Based on the analysis of the tortuosity during the gas flow process investigated in Section 4.2, when the initial fracture angles are 15°, 75°, and 90°, the fracture surface undulations are highly concentrated. During the gas flow process, the gas mainly flows through certain height variations, leading to low flow tortuosity. Consequently, the gas collides and experiences less friction with the fracture surface, leading to a small pressure exerted on the surface of the fracture channel. Conversely, when there is no initial fracture or initial angles are 30°, 45°, and 60°, the gas encounters multiple undulations during its flow in the fracture channel, leading to high tortuosity. Thus, the gas frequently collides with the fracture surface during flow, resulting in high pressure on the fracture surface.

$$P_{\text{nor}} = \left(1 - \frac{\text{Max}(P) - P_n}{\text{Max}(P) - \text{Min}(P)}\right) \times 100\% \qquad (6)$$

where P_{nor} is the pressure after normalization, %; Max(P) the maximum value of the pressure applied to all the fracture surfaces, Pa; Min(P) the minimum value of the pressure applied to all the frac-

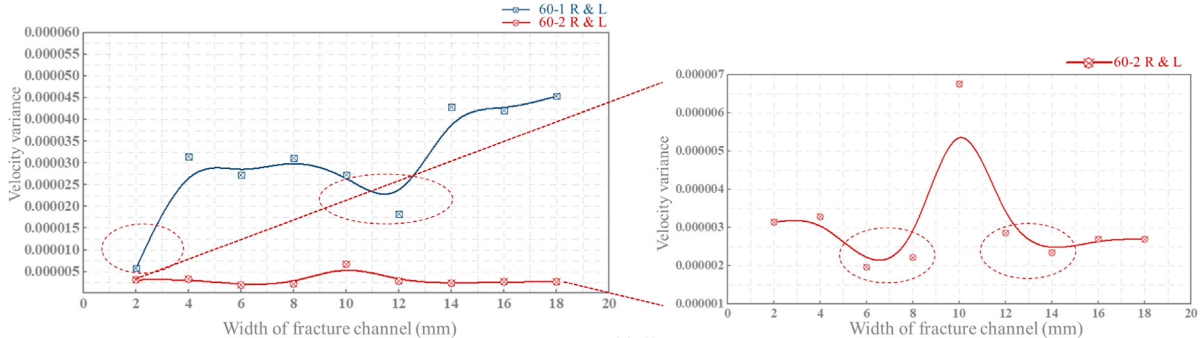

(g) 60

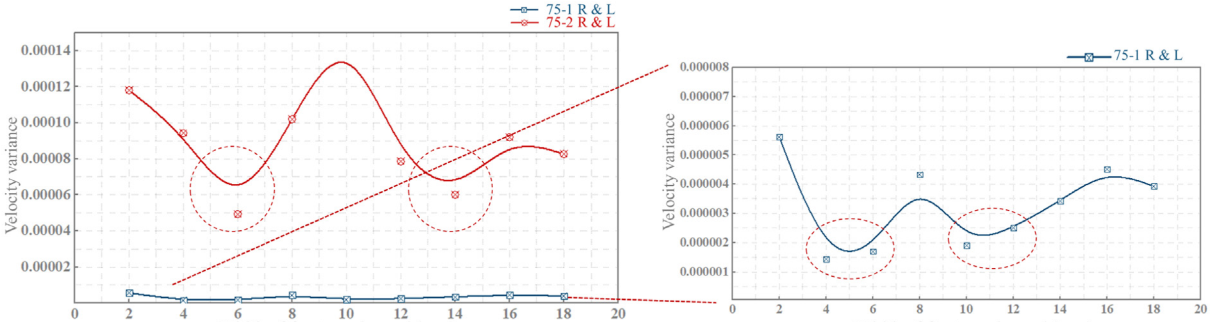

(h) 75

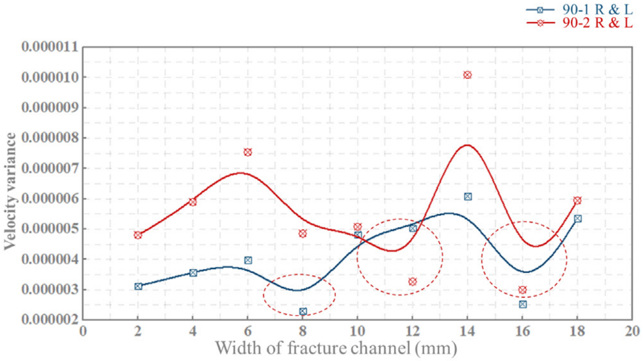

(I) 90

Fig. 15 (*continued*)

ture surfaces, Pa; P_n the stress applied to the fracture surfaces, Pa; and n the initial fracture angle, 0°, 15°, 30°, 45°, 60°, 75°, and 90°.

4.3.3. Gas flow velocity response characteristics to fracture surface meshing degree

Upon further comparison of the gas flow within the fracture channels, it can be observed that even when the gas passes through fracture channels formed with the same initial fracture angle, velocity disparities persist. Taking the 15° initial angle as an example, the maximum flow velocities of fracture channel 15–1 (R & L) and fracture channel 15–2 (R & L) were 0.074 and 0.091 m/s, respectively. This demonstrates that the meshing degree of a channel's two fracture surfaces may also disturb gas flow. Hence, according to the quantitative analysis results of the fracture surface in Section 4.1 (Table 3), the variance difference between the fracture surfaces of each fracture channel was calculated, as shown in Eq. (7), and the calculation result is used as the meshing degree of the fracture surfaces of the channel. The theory of the meshing equation states that if two surfaces are highly meshed, the change in the height of undulation in their surfaces is convergent. Since the variance of fracture surface undulation height can characterize the change in undulation height, similar variances imply high meshing. Therefore, in Eq. (7), the difference between the variances of the two surfaces is used to characterize the consistency of the change in the undulation of the two fracture surfaces. When the two surfaces mesh well, their undulation change evolution laws are similar: the smaller the variance difference in undulation changes, the better the similarity in undulation and meshing of the fracture channel. The meshing degrees of the different fracture channels and the maximum gas flow velocities in the fracture channels are shown in Fig. 18.

$$V_n = |V_R - V_L| \tag{7}$$

where V_n is the meshing degree of the fracture surfaces; V_R the variance of the undulation of the R surface; and V_L the variance of the undulation of the L surface.

The larger the meshing degree value, the worse the meshing condition, indicating substantial disparity in undulation between

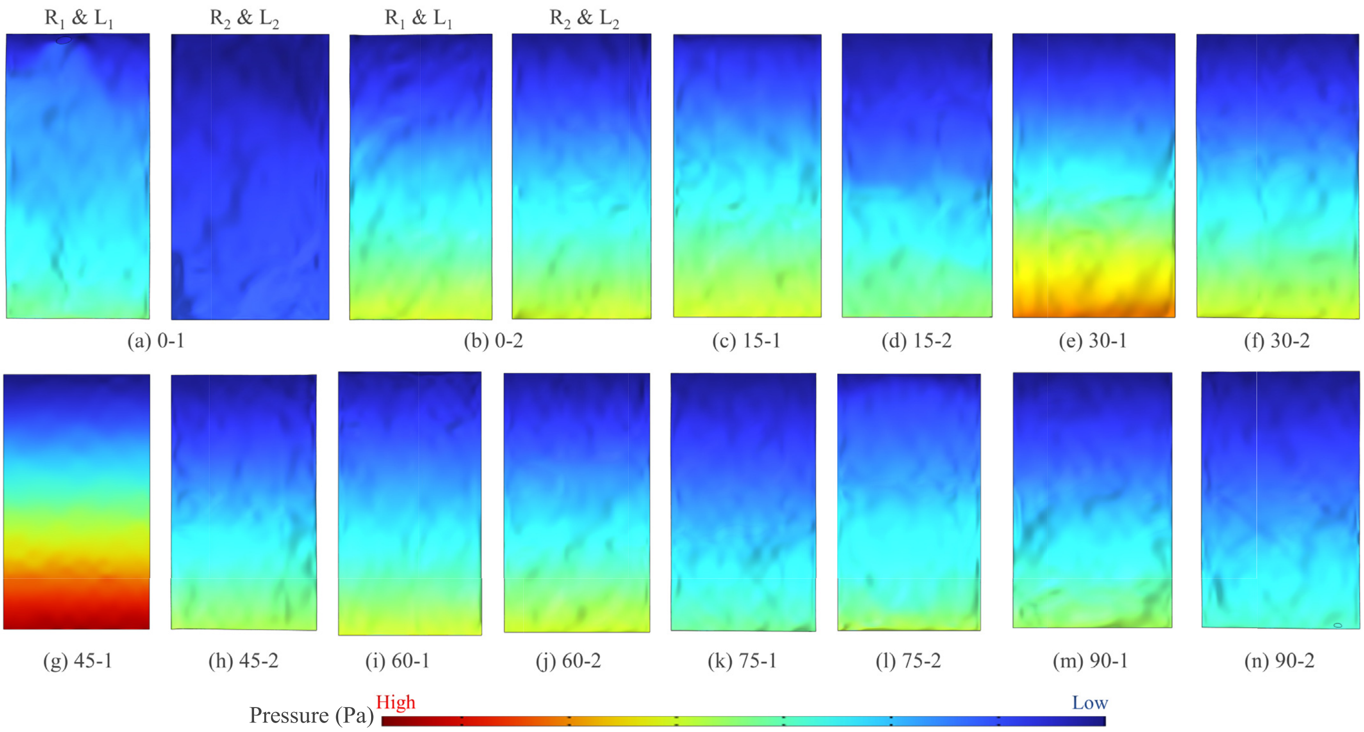

Fig. 16. Pressure cloud maps of fracture channels.

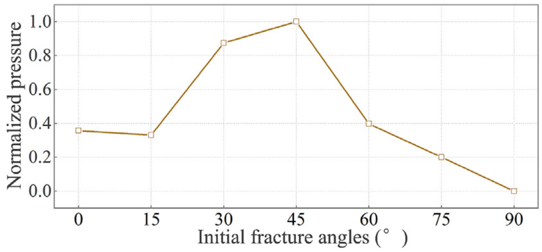

Fig. 17. Normalized maximum pressure of each fracture channel.

the fracture surfaces. In contrast, the smaller the meshing degree value, the better the meshing condition. Currently, the consistency of the undulation between the fracture surfaces is much higher. As shown in Fig. 18, the maximum gas flow velocities in different fracture channels are affected by the respective fracture surfaces. An overall positive correlation is observed between the meshing degree of the fracture surface and the maximum flow velocity. Specifically, for fracture channels with the same initial fracture angle, the maximum velocity in the fracture channels with a higher meshing degree exceeds that in channels with a lower meshing degree. This result indicates that the gas flow velocity changes significantly when the meshing degree between the two fracture surfaces is low, which is because factors such as friction between rocks come into play during the rock fracturing process. The fracture surfaces may be worn, causing fine particles on the surface to shed. Consequently, there are certain differences in the undulation, even between fracture surfaces formed by the same fracture channel. As shown in Fig. 19a, large undulation differences (poor meshing) create channel size variations due to uneven surface undulations. The worse the meshing, the more significant change in channel size, which affects gas flow velocity [30]. Thus, low-meshing channels exhibit substantial velocity variations and large

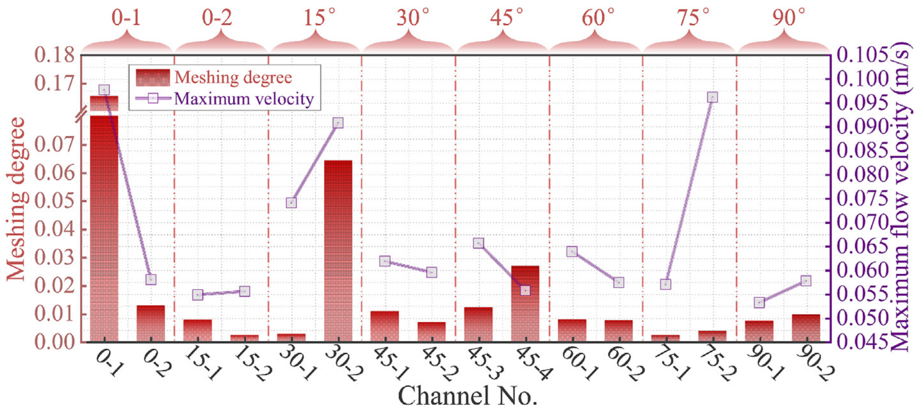

Fig. 18. Fracture surface meshing degrees and maximum gas flow velocities.

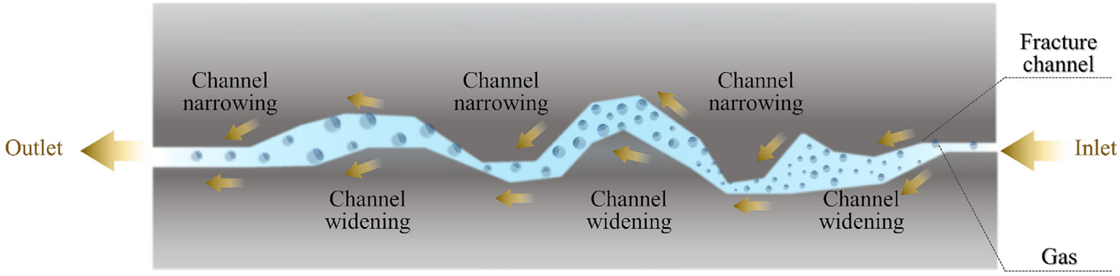

(a) Low meshing degree channel

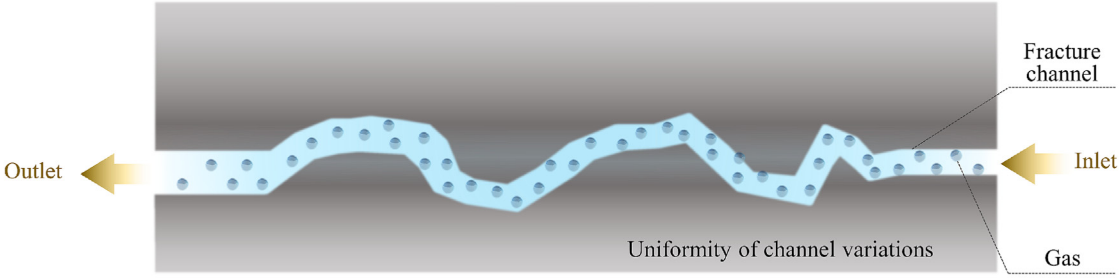

(b) High meshing degree channel

Fig. 19. Fracture channels at different meshing degrees.

velocity differences. In contrast, similar undulations between surfaces (good meshing, Fig. 19b) result in negligible disruptions to the channel size, ensuring a stable gas flow velocity in the channel.

5. Conclusions

This study aims to investigate the gas flow guiding mechanism of rock fracture channels and establish a correlation between fracture surface undulations and gas-guiding capability. To achieve this, four-point bending tests were conducted on rocks with prefabricated fractures at different angles under stable stepped stress loading. Several key indexes of the fracture surface, such as relative undulation intensity, undulation frequency, and meshing degree, were proposed. These indexes enabled a quantitative description of the directivity, tortuosity, and uniformity of the gas flow within the fracture channels based on the roughness of the fracture surfaces. Subsequently, numerical models were established to validate the effectiveness of the proposed indexes.

(1) The undulation of the fracture surface is delineated using an initial fracture angle of 45°. When the initial fracture angle is less than 45°, it falls within the high undulation range; when it is greater than 45°, it falls within the low undulation range. Considering the relative undulation degree of the fracture surface, during the non-fracture stage of the fracture channel, the gas flow is stable at one side of the fracture surface. When the initial fracture angle ranged from 15° to 45°, the gas flow is stable at the middle of the fracture surface. When the initial fracture angle is between 60° and 90°, a large area of stable gas flow velocity is observed.

(2) The undulation frequency of the rock fracture surface serves as an indicator for assessing the tortuosity of the gas flow in the fracture channel. When the undulation of the fracture surface is highly concentrated during flow, the gas has to overcome the height variation at a local portion of the fracture surface, resulting in low tortuosity. The extent of collision and friction between the gas and fracture surface during the flow is minimal, and the pressure exerted on the surface of the fracture channel is low as well. In contrast, if the undulation changes of the fracture surface are dispersed, with each of the different undulation intervals having a certain proportion, and these proportions are approximately the same, the gas should flow multiple undulation intervals. Consequently, the tortuosity is high due to the high density, and the gas frequently collided with the surface of the fracture channel during flow, causing the surface of the fracture channel to be subjected to greater pressure.

(3) The meshing degree between the two fracture surfaces can disrupt the gas flow process, thereby affecting the uniformity of the gas flow. The meshing degree refers to the degree of the undulation between two fracture surfaces of the same channel. The closer the undulation profiles of the two surfaces, the better their meshing degree. When the meshing degree between the two fracture surfaces of the fracture channel is poor, the gas flow velocity changes significantly, leading to low uniformity. The uniformity of gas flow in a fracture channel with good meshing is higher than that in one with poor meshing.

Acknowledgments

This work was financially supported by the National Natural Science Foundation of China (No. 52522405) and Henan Provincial Natural Science Foundation (No. 252300421323).

References

[1] Ran QC, Liang YP, Yang ZL, Zou QL, Ye CF, Tian CL, Wu ZP, Zhang BC, Wang WZ. Deterioration mechanisms of coal mechanical properties under uniaxial multi-level cyclic loading considering initial damage effects. Int J Rock Mech Min Sci 2025;186:106006.

[2] Xu JL, Qian MG. Study and application of dominant stratum theory for control of strata movement. China Min Mag 2001;10(6):54–6. in Chinese.

[3] Zhang BC, Liang YP, Zou QL, Ding LQ, Ran QC. Experimental investigation into the damage evolution of sandstone under decreasing-amplitude stress rates and its implications for coalbed methane exploitation. Environ Earth Sci 2023;82(9):208.

[4] Feng MS. Research on overburden rock breaking law in shallow coal mining. Doctoral dissertation. Fuxin: Liaoning Technical University; 2014. in Chinese.

[5] Karacan CÖ. Modeling and analysis of gas capture from sealed sections of abandoned coal mines. Int J Coal Geol 2015;138:30–41.

[6] Huang P, Zhang JX, Yan XJ, Spearing AJS, Li M, Liu SW. Deformation response of roof in solid backfilling coal mining based on viscoelastic properties of waste gangue. Int J Min Sci Technol 2021;31(2):279–89.

[7] Chen ZH, Zou QL, Gao SK, Zhan JF, Chen CM, Ran QC, Sun XY. Long-term evolution of overlying rock fractures in mined-out areas and its effect on gas flow conductivity. Fuel 2023;353:129213.

[8] Jiang XY, Wu D, Zhao ZX, Yang Y, Tian JW, Wang FL. Experimental and numerical study on the damage evolution and acoustic emission multi-parameter responses of single flaw sandstone under uniaxial compression. Theor Appl Fract Mech 2024;133:104535.

[9] Wang J, Zhu WS, Ma HP. Crack propagation of jointed rock and application. Appl Mech Mater 2011;117–119:476–9.

[10] Zhou J, Wang KZ, Zhou WD, Yao YL, Xie T. Uniaxial compressive damage characteristics of rock-like materials with prefabricated conjugate cracks. Appl Sci 2024;14(2):823.

[11] Huang YH, Wu SY, Yang C. Experimental study on the failure behaviors of sandstone specimens with two fissures under triaxial loading and unloading conditions. Eng Fract Mech 2024;298:109933.

[12] Li B, He YZ, Li L, Zhang JX, Shi Z, Zhang YP. Damage evolution of rock containing prefabricated cracks based on infrared radiation and energy dissipation. Theor Appl Fract Mech 2023;125:103853.

[13] Mu K, Zhang MH, Yu J. Study on stress relaxation and acoustic emission of fractured rocks with different fissure inclinations. Case Stud Constr Mater 2024;20.

[14] Salmi EF, Malinowska A, Hejmanowski R. Investigating the post-mining subsidence and the long-term stability of old mining excavations: Case of Cow Pasture Limestone Mine, West Midlands. UK Bull Eng Geol Environ 2020;79(1):225–42.

[15] Xia BW, Ma ZK, Hu HR, Li Y, Zhao WM. A prediction method of stress intensity factor for mode-I crack in coal rock based on deep learning. Theor Appl Fract Mech 2022;122:103645.

[16] Lu YL, Li WS, Wang LG, Meng XY, Wang B, Zhang KW, Zhang XD. *In-situ* microscale visualization experiments on microcracking and microdeformation behaviour around a pre-crack tip in a three-point bending sandstone. Int J Rock Mech Min Sci 2019;114:175–85.

[17] Sarkar S, Kumar R, Murthy VMSR. Experimental and numerical simulation of crack propagation in sandstone by semi circular bend test. Geotech Geol Eng 2019;37(4):3157–69.

[18] Gao YN, Shao XS, Wang YL, Hou P, Gao MZ. Does double pre-notches have a greater impact than single pre-Notch on the mechanical and fracture behavior of rock? Insights from three-point bending tests using the numerical approach of grain-based model. Theor Appl Fract Mech 2024;133:104624.

[19] Shah KS, Bin Mohd Hashim MH, Emad MZ, Bin Ariffin KS, Junaid M, Khan NM. Effect of particle morphology on mechanical behavior of rock mass. Arab J Geosci 2020;13(15):708.

[20] Zhou AT, Xu ZY, Wang K, Liu YF, Feng YF, Zhu ZB. Experimental and numerical analysis of high-pressure gas-driven rock particle impact and fragmentation rock technology. Phys Fluids 2024;36(12):126614.

[21] Li B, Mo YY, Zou LC, Liu RC, Cvetkovic V. Influence of surface roughness on fluid flow and solute transport through 3D crossed rock fractures. J Hydrol 2020;582:124284.

[22] Crandall D, Bromhal G, Karpyn ZT. Numerical simulations examining the relationship between wall-roughness and fluid flow in rock fractures. Int J Rock Mech Min Sci 2010;47(5):784–96.

[23] Isrm. Suggested methods for the quantitative description of discontinuities in rock masses. Int J Rock Mech Min Sci Geomech Abstr 1979;16(2):22.

[24] Li BX, Zhang WM, Xue YG, Li ZQ, Kong FM, Kong R, Wang G. Approach to characterize rock fracture surface: Insight from roughness and fractal dimension. Eng Geol 2023;325:107302.

[25] Li BX, Zhang WM, Xue YG, Kong R, Zhu WS, Yu YH, Chen YJ. An image segmentation-based method for quantifying the rock failure mechanism under true triaxial compression. Int J Rock Mech Min Sci 2022;158:105195.

[26] Wu CZ, Chu J, Wu SF, Hong Y. 3D characterization of microbially induced carbonate precipitation in rock fracture and the resulted permeability reduction. Eng Geol 2019;249:23–30.

[27] Razavi N, Aliha MRM, Berto F. Application of an average strain energy density criterion to obtain the mixed mode fracture load of granite rock tested with the cracked asymmetric four-point bend specimens. Theor Appl Fract Mech 2018;97:419–25.

[28] Yang XJ, Zhang WR, Xue DJ, Tao ZG, Xi SD. Seepage analysis of orthogonal shear cracks in granite based on fractal theory. Geotech Geol Eng 2022;40(1):425–41.

[29] Yang K, Li W, Gao L, Wang HF, Liu JZ, Lin J. Multiscale transport characteristics of coalbed methane in abandoned mines and its applications in gas recovery. Nat Resour Res 2023;32(4):1621–37.

[30] Zou QL, Chen ZH, Zhan JF, Chen CM, Gao SK, Kong FJ, Xia XF. Morphological evolution and flow conduction characteristics of fracture channels in fractured sandstone under cyclic loading and unloading. Int J Min Sci Technol 2023;33(12):1527–40.